

# <sup>1</sup> **Global inter-comparison of 12 land surface heat flux** <sup>2</sup> **estimates**

C. Jiménez,<sup>1</sup> C. Prigent,<sup>1</sup> B. Mueller,<sup>2</sup> S. I. Seneviratne,<sup>2</sup> M. F. McCabe,<sup>3</sup> E.  
F. Wood,<sup>4</sup> W. B. Rossow,<sup>5</sup> G. Balsamo,<sup>6</sup> A. K. Betts,<sup>7</sup> P. A. Dirmeyer,<sup>8</sup> J. B.  
Fisher,<sup>9</sup> M. Jung,<sup>10</sup> M. Kanamitsu,<sup>11</sup> R. H. Reichle,<sup>12</sup> M. Reichstein,<sup>10</sup> M.  
Rodell,<sup>13</sup> J. Sheffield,<sup>4</sup> K. Tu,<sup>14</sup> K. Wang,<sup>15</sup>

---

C. Jiménez, Laboratoire d'Etudes du Rayonnement et de la Matière en Astrophysique,  
Centre National de la Recherche Scientifique, Observatoire de Paris, Paris, France (car-  
los.jimenez@obspm.fr)

<sup>1</sup>Laboratoire d'Etudes du Rayonnement

**Abstract.**

A global inter-comparison of 12 monthly mean land surface heat flux products for the period 1993-1995 is presented. The inter-comparison includes some of the first emerging global satellite-based products (developed at Paris Observatory, MPI for Biogeochemistry, University of California Berkeley, University of Maryland, and Princeton University) and examples of fluxes produced by reanalyses (ERA-Interim, MERRA, NCEP-DOE) and off-line land surface models (GSWP-2, GLDAS CLM/Mosaic/Noah). An inter-comparison of the global latent heat flux ( $Q_{le}$ ) annual means shows a spread of  $\sim 20 \text{ W m}^{-2}$  (all-product global average of  $\sim 45 \text{ W m}^{-2}$ ). A similar spread is observed for the sensible ( $Q_h$ ) and net radiative ( $R_n$ ) fluxes. In general, the products correlate well with each other, helped by the large seasonal variability and common forcing data for some of the products. Expected spatial distributions related to the major climatic regimes and geographical features are reproduced by all products. Nevertheless, large  $Q_{le}$  and  $Q_h$  absolute differences are also observed. The fluxes were spatially averaged for 10 vegetation classes. The larger  $Q_{le}$  differences were observed for the rain forest, but when normalized by mean fluxes the differences were comparable to other classes. In general, the correlations between  $Q_{le}$  and  $R_n$  were higher for the satellite-based products compared with the reanalyses and off-line models. The fluxes were also averaged for 10 selected basins. The seasonality was generally well

---

et de la Matière en Astrophysique, Centre

24 captured by all products, but large differences in the flux partitioning were  
25 observed for some products and basins.

---

National de la Recherche Scientifique,

## 1. Introduction

26 Land surface heat fluxes are essential components of the water and energy cycles and  
27 govern the interactions between the Earth surface and the atmosphere [e.g., *Betts et al.*,  
28 1996]. Variables such as cloud cover, precipitation, surface radiation, or air temperature  
29 and humidity, which are related to the atmospheric synoptic patterns and meso-scale  
30 structures, strongly influence the fluxes. In turn, the energy balance at the surface and  
31 its partitioning between the turbulent sensible ( $Q_h$ ) and latent ( $Q_{le}$ ) heat fluxes (here  
32 collectively referred as  $Q$ ) also affect the atmosphere, determining the development of  
33 the atmospheric boundary layer [e.g., *Viterbo and Beljaars*, 1995]. Over land, energy  
34 balance and flux partitioning are complex mechanisms, with strong variability in both  
35 space and time, across climates and ecosystems, and in relation to the physical properties  
36 of the surface, especially moisture availability and vegetation. *In situ* measurements of  
37 land surface heat fluxes are available from field experiments (e.g., the Boreal Ecosystem-  
38 Atmosphere Study (BOREAS) [*Sellers et al.*, 1997]) and from some flux tower networks  
39 (e.g. FLUXNET [*Baldocchi et al.*, 2001]), but in order to obtain global, consistent es-  
40 timates of  $Q$  a transition to satellite remote sensing is needed. The challenge is that  
41 heat fluxes produce neither absorption nor emission of electromagnetic signals directly.  
42 Therefore, observations related to surface temperature, soil moisture, or vegetation have  
43 to be combined with an interpretive model to derive the fluxes.

44 The currently available datasets were grouped based on the degree of complexity of  
45 the model used to derive  $Q$ . A first group includes the estimates derived from relatively

---

Observatoire de Paris, Paris, France.

46 simple models dedicated primarily to deriving the fluxes using remote sensing and me-  
47 teorological inputs. Different methodologies exist, including empirical models that link  
48 the remote sensing observations to measured or modelled fluxes [e.g., *Wang et al.*, 2007b;  
49 *Jiménez et al.*, 2009], schemes using remotely sensed land surface temperature as the main  
50 boundary condition of a surface energy balance model [e.g., *Su*, 2002; *Anderson and Kus-*  
51 *tas*, 2008], or algorithms based on the equations predicting the main evapotranspiration  
52 processes [e.g., *Nishida et al.*, 2003; *Leuning et al.*, 2008]. Despite a large body of work,  
53 it is only recently that this capability has started to be adopted at the global scale. Diffi-  
54 culties arise from the fact that even relatively simple parameterizations may require large  
55 amounts of ancillary data that are not available globally (such as surface roughness to  
56 characterize heat transfer processes, or surface meteorological data to drive evaporation  
57 processes), making it difficult to extend from the local or regional scale to the global scale.  
58 In fact, at the moment most methodologies cannot solely rely on remote sensing obser-  
59 vations, so that datasets derived from meteorological *in situ* measurements [e.g., *Fisher*  
60 *et al.*, 2008] or analyses [e.g., *Mu et al.*, 2007; *Gellens-Meulenberghs et al.*, 2007] are also  
61 needed to provide the required inputs to the models. Nevertheless, clear progress has been  
62 made in the recent years, and first global estimates of  $Q$  are now available [e.g., *Fisher*  
63 *et al.*, 2008; *Wang and Liang*, 2008; *Jiménez et al.*, 2009] . These estimates are referred  
64 to here as satellite-based products, to emphasize the fact that their estimates are derived  
65 by relatively simple formulation/models relying to a large extent on diagnostic satellite  
66 observations.

---

<sup>2</sup>Institute for Atmospheric and Climate

67 A second group includes the Q estimates produced by more complex land surface mod-  
68 els that are constructed to provide a more complete characterization of surface energy  
69 and water budget processes. The land surface model can be coupled with an atmospheric  
70 model that assimilates observational data, such as in the weather reanalyses [e.g., *Ek*  
71 *et al.*, 2003; *Balsamo et al.*, 2009], or can be forced off-line by observational or model  
72 data [e.g., *Dirmeyer et al.*, 2006; *Boone et al.*, 2009]. There is also work towards the  
73 assimilation of surface observations [e.g., *Rodell et al.*, 2004]. Before the emergence of  
74 the first global satellite-based products, the only source of Q with adequate time and  
75 space samplings came from the land surface models. However, inter-comparisons of the  
76 land surface model outputs showed very large differences, due to model parameterizations  
77 and forcings (e.g., the Project to Intercompare Land-Surface Parameterization Schemes  
78 (PILPS) [*Henderson-Sellers et al.*, 1995] and the Global Soil Wetness Project (GSWP)  
79 version 1 and 2 [*Entin et al.*, 1999; *Dirmeyer et al.*, 2006]). Land surface model pa-  
80 rameterizations are often developed empirically and tuned to local conditions where the  
81 ancillary data needed to estimate the model parameters are measured [e.g., *Wilson et al.*,  
82 2002; *Wright et al.*, 1995]. Some parameters, such as fractional vegetation cover or leaf  
83 area index, can be estimated from satellites, but many other parameters are derived from  
84 approximate relationships with vegetation, soil type, or climate regime. To aid the dis-  
85 cussion, the estimates from the second group are further divided into two sub-groups,  
86 referred to here as “reanalyses” (the coupled land surface models) and “off-line models”  
87 (the land surface models forced off-line), even if it is clear that the reanalysis estimates  
88 also come from a land surface model, and that many off-line forcing datasets are based

---

Science, ETH Zurich, Zurich, Switzerland.

89 on reanalysis estimates (which are sometimes corrected towards observations not used in  
90 the reanalysis).

91 Evaluating global Q estimates is difficult. This is not specific for the fluxes, since other  
92 major components of the hydrological cycle, such as soil moisture or precipitation, are  
93 also difficult to evaluate [e.g., *Grubber and Levizzani, 2008; Prigent et al., 2005; Senevi-*  
94 *ratne et al., 2010*]. By using tower flux measurements, formulations and models can be  
95 evaluated at the tower scale by using a combination of the surface meteorology from the  
96 station and, if relevant, the satellite forcing (if the resolution is compatible with the tower  
97 measurements) [e.g., *McCabe and Wood, 2006; Su et al., 2007; Cleugh et al., 2007; Fisher*  
98 *et al., 2008; Stöckli et al., 2008*]. The tower data representativity and quality should also  
99 be considered [e.g., *Williams et al., 2009*]. Once the models are driven by global datasets,  
100 an evaluation with tower fluxes is more questionable due to the scale miss-match between  
101 satellite retrievals, model outputs, and tower observations, and the coverage of the tower  
102 network. A qualitative examination of the fluxes, by checking the consistency displayed  
103 between the Q estimates and independent but related hydrological observations has also  
104 been proposed [e.g., *McCabe et al., 2008*].

105 Global inter-comparison of Q between reanalyses [e.g., *Betts et al., 2006; Bosilovich*  
106 *et al., 2009*], off-line models forced with the same datasets [e.g., *Schlosser and Gao, 2009*],  
107 or climate model simulations [e.g., *Lim and Roderick, 2009*] have already been presented.  
108 To the best of our knowledge, no systematic inter-comparison that also includes satellite-  
109 based products at the global scale has yet been published. In the framework of the Global

---

<sup>3</sup>School of Civil and Environmental

110 Energy and Water Cycle Experiment (GEWEX) Radiation Panel (GRP) LandFlux ac-  
111 tivity, such inter-comparison has been initiated under the dedicated LandFlux-EVAL ini-  
112 tiative. LandFlux aims at providing a framework for undertaking coordinated evaluation  
113 and assessment of the emerging global flux products, ultimately identifying and delivering  
114 a robust procedure for the operational production of a global land surface flux dataset to  
115 improve climate scale water and energy cycle characterization. Together with a paper by  
116 *Mueller et al.* (in preparation) focusing only on evapotranspiration estimates but for a  
117 larger number of products (including estimates from climate models participating in the  
118 Intergovernmental Panel on Climate Change Fourth Assessment Report (IPCC-AR4)),  
119 this publication presents the first results of the LandFlux-EVAL initiative. The period  
120 chosen for this analysis is 1993-1995 (1986-1995 in *Mueller et al.*, in preparation), the  
121 final three years of the GSWP-2 exercise and the first three years of the estimates from  
122 Paris Observatory. Although analysis of shorter time scales would be desirable, at the  
123 moment most of the available global estimates from satellite-based products are limited  
124 to monthly averages by the time sampling of the available forcings. As satellite-based  
125 products, estimates provided by the University of California, the University of Maryland,  
126 Paris Observatory, Princeton University, and the Max Planck Institute for Biochemistry,  
127 are included in the inter-comparison. As reanalyses, estimates from the The Modern  
128 Era Retrospective-analysis for Research and Applications (MERRA), the National Cen-  
129 ters for Environmental Prediction-Department of Energy (NCEP/DOE) reanalysis R-2,  
130 and the European Centre for Medium-Range Weather Forecasts (ECMWF) ERA-Interim  
131 reanalysis are considered. As off-line models, estimates from the multi-model ensemble

---

Engineering, University of New South



132 GSWP-2 and from the land surface models Mosaic, Noah and Community Land Model  
133 (CLM) driven by the Global Land Data Assimilation System (GLDAS) are presented.  
134 The choice of products is based on a desire to have a representative sample of different  
135 approaches. For the off-line models, the GSWP-2 multi-model ensemble is a representa-  
136 tive example of multi-model outputs, while the GLDAS runs provide a good example of  
137 fluxes from individual models that were forced with the same datasets.

138 This paper focuses on an inter-comparison of the selected fluxes. There is no attempt  
139 to quantify the accuracy of the products, or to claim that one product is superior to the  
140 others. The goal is to highlight the differences between the products in order to evaluate  
141 the range of the existing global Q estimates. The paper is structured as follows. Section 2  
142 presents the different modeling frameworks. Section 3 explains the spatial and temporal  
143 aggregation of the datasets that enables the inter-comparison. Sections 4.1 and 4.2 present  
144 the differences in the global yearly and seasonal Q averages. Sections 4.3 inter-compares  
145 spatially averaged fluxes for major vegetation classes. Section 4.4 inter-compares spatially  
146 averaged fluxes for a group of selected basins. Finally, Section 5 gives the summary and  
147 conclusions. The paper is complemented by a collection of additional figures, denoted in  
148 the text with a capital S. They can be found in the auxiliary material accompanying the  
149 paper.

## 2. Data

---

Wales, Sydney, Australia.

## 2.1. Satellite-based products

150 The different flux and auxiliary products are described below. The products will be  
 151 referred to in the text by the first short name given after the product name (e.g., PA-OBS  
 152 for Paris Observatory). To avoid cluttering in the legends, the products will be referred  
 153 in the tables and figures as the second (smaller) short name (e.g. PAO for the given  
 154 example). A summary of the products is given in Table 1.

### 155 2.1.1. University of California Berkeley [UCB,UCB]

156  $Q_{le}$  is estimated from a bio-meteorological approach that translates Priestley-Taylor  
 157 estimates of potential evapotranspiration into rates of actual evapotranspiration [*Fisher*  
 158 *et al.*, 2008, 2009]. The method was evaluated at the local scale at 36 FLUXNET sites  
 159 across 2 years, and has been extended to estimate global  $Q_{le}$  by forcing the model with  
 160 the International Satellite Land Surface Climatology Project, Initiative II (ISLSCP-II)  
 161 datasets [*Hall et al.*, 2006]. Main inputs are the radiative fluxes ( $R_N$ ) from the GEWEX  
 162 Surface Radiation Budget (GEWEX-SRB) [*Stackhouse et al.*, 2004], maximum air temper-  
 163 ature and vapor pressure from the Climate Research Unit (CRU) [*New et al.*, 1999, 2000],  
 164 and a vegetation characterization using the Advance Very High Resolution Radiometer  
 165 (AVHRR) reflectances [*Gutman*, 1999; *Huete*, 1998] processed as the Fourier-Adjusted,  
 166 Sensor and Solar zenith angle corrected, Interpolated, Reconstructed (FASIR) Normalized  
 167 Difference Vegetation Index (NDVI) [*Los et al.*, 2000]. The spatial resolution is  $0.5^\circ \times 0.5^\circ$ ,  
 168 and monthly averaged values in  $mm\ month^{-1}$  are available from 1986 to 1995.

### 169 2.1.2. University of Maryland [UMD, UMD]

---

<sup>4</sup>Department of Civil and Environmental

170  $Q_{le}$  is estimated from a statistical approach that locally relates (by linear regression)  $R_n$ ,  
 171 near-surface air temperature, surface temperature, and a vegetation index with observed  
 172 Energy Balance Bowen Ratio (EBBR)  $Q_{le}$  at eight sites over the Southern Great Plains  
 173 [*Wang and Liang, 2008*]. The method was evaluated at local scale at AmeriFlux stations  
 174 across 4 years, and extended to estimate global  $Q_{le}$  by forcing the model with ISLSCP-II  
 175 datasets. Inputs are the  $R_n$  (GEWEX-SRB), daily averaged and diurnal range of the  
 176 air temperature (CRU), and a vegetation index from AVHRR reflectances. An improved  
 177 model that explicitly includes the impact of wind speed and water vapor pressure deficit  
 178 to improve its capability in modeling climate variability of  $Q_{le}$  has just been developed  
 179 [*Wang et al., 2010a, b*], but the estimates included here correspond to the model presented  
 180 in *Wang and Liang [2008]*. The spatial resolution is  $1^\circ \times 1^\circ$ , and monthly mean values in  
 181  $W m^{-2}$  from 1986 to 1995 are available.

### 182 **2.1.3. Paris Observatory [PA-OBS, PAO]**

183  $Q_{le}$  and  $Q_h$  are estimated from a statistical approach that globally relates (using non-  
 184 linear regression) a suite of multi-frequency remote sensing observations with modeled  
 185 fluxes from the GSWP-2 multi-model ensemble [*Jiménez et al., 2009*]. The statistical  
 186 model is driven by the following inputs: reflectances from AVHRR, land surface temper-  
 187 ature and its diurnal cycle from the International Satellite Cloud Climatology Project  
 188 (ISCCP) [*Rossow and Schiffer, 1999; Aires et al., 2004*], active microwave backscatter  
 189 from the European Remote-sensing Satellite (ERS) scatterometer [*Francis et al., 1991;*  
 190 *Frison and Mougin, 1996*], and passive microwave emissivities from the Special Sensor  
 191 Microwave/Imager (SSM/I) [*Hollinger et al., 1987; Prigent et al., 2006*]. The approach

---

Engineering, Princeton University,

192 was evaluated at local scale at AmeriFlux stations. The spatial resolution is  $0.25^\circ \times 0.25^\circ$   
193 (at the equator), and monthly mean values in  $W m^{-2}$  of  $Q_{le}$  and  $Q_h$  are currently available  
194 from 1993 to 1999.

#### 195 **2.1.4. Princeton University [PRU, PRU]**

196  $Q_{le}$  is estimated from a modified version of the Penman-Monteith algorithm described  
197 in *Sheffield et al.* [2009]. For global application, the formulation is driven by ISCCP  $R_n$   
198 and near surface air and surface temperature, reanalysis wind speed [*Sheffield et al.*, 2006],  
199 and vegetation characterization from AVHRR reflectances. The approach was evaluated  
200 over Mexico with global forcings down-scaled for this region using data from the North  
201 American Regional Analysis (NARR) [*Mesinger et al.*, 2006]. The spatial resolution is  
202  $2.5^\circ \times 2.5^\circ$ , and daily mean values in  $mm day^{-1}$  are available from 1986 to 2006.

#### 203 **2.1.5. Max Planck Institute for Biogeochemistry [MPI-BGC, MPI]**

204  $Q_{le}$  and  $Q_h$  are estimated by a global upscaling of eddy covariance (EC) measurements  
205 from FLUXNET by a machine learning approach called model tree ensembles (MTE)  
206 [*Jung et al.*, 2009]. The EC measurements used are part of the FLUXNET LaThuille  
207 synthesis data set, which was established by a standard processing according to *Reichstein*  
208 *et al.* [2005] and *Papale et al.* [2006] and comprises  $\sim 950$  years of data from  $\sim 250$  sites.  
209 The EC measurements are corrected to force energy balance closure on a monthly time  
210 scale. The global upscaling is driven by a long-term monthly fraction of absorbed pho-  
211 tosynthetically active radiation (fAPAR) dataset (established by harmonizing AVHRR  
212 NDVI data [*Vermote and Saleous*, 2005] with fAPAR from SeaWiFS [*Gobron et al.*, 2006]  
213 and fAPAR from MERIS [*Gobron et al.*, 2008]), near surface air temperature from CRU,

---

Princeton New Jersey, USA.

214 precipitation data from the Global Precipitation Climatology Center (GPCC) [*Rudolf and*  
215 *Schneider, 2005*], and an estimation of the top of the atmosphere shortwave radiation.  
216 The product was evaluated against river runoff data and the GSWP-2 multi-model ensem-  
217 ble. The spatial resolution is  $0.5^\circ \times 0.5^\circ$ , and monthly mean values in  $W m^{-2}$  are available  
218 from 1982 to 2008. For simplicity this product is included as a satellite-based product,  
219 but notice that this product is to a large extent based on in-situ datasets.

## 2.2. Reanalyses

### 2.2.1. ERA Interim reanalysis [ERA-INT, ERA]

220 ERA-Interim is a new global reanalysis from the European Centre for Medium-Range  
221 Weather Forecasts (ECMWF) [*Simmons et al., 2006*], focusing on the data-rich period  
222 since 1989. The ERA-Interim system is based on a recent release of the Integrated Fore-  
223 casting System (IFS Cy31r2), released operationally in September 2006, containing many  
224 improvements both in the forecasting model and analysis methodology. The surface fluxes  
225 in ERA-Interim are based on the land surface model TESSEL (Tiled ECMWF Surface  
226 Scheme for Exchange over Land, [*van den Hurk et al., 2000*]) forced by atmospheric anal-  
227 ysis and short range forecasts. A land data assimilation constrains the model fields on  
228 the basis of short range forecast errors: soil moisture and soil temperature are corrected  
229 using air temperature and relative humidity observations from SYNOP stations [*Douville*  
230 *et al., 2000*]; snow mass errors are constrained by SYNOP snow depth reports and satel-  
231 lite snow cover data [*Drusch et al., 2004*]. The fluxes were obtained as monthly mean  
232

---

<sup>5</sup>NOAA-Cooperative Remote Sensing

233 values in  $W m^{-2}$  at a resolution of  $3/4^{\circ} \times 3/4^{\circ}$  (very close to the native ERA-Interim  
234 T255 Gaussian reduced grid).

### 235 **2.2.2. MERRA reanalysis [MERRA, MER]**

236 The Modern Era Retrospective-analysis for Research and Applications (MERRA) is a  
237 National Aeronautics and Space Administration (NASA) reanalysis for the satellite era  
238 using a major new version of the Goddard Earth Observing System Data Assimilation  
239 System Version 5 (GEOS-5) [Bosilovich, 2008]. The project focuses on historical analyses  
240 of the hydrological cycle on a broad range of weather and climate time scales and places  
241 the NASA EOS suite of observations in a climate context. The monthly flux averages  
242 in  $W m^{-2}$  were downloaded from the MERRA data archive at a spatial resolution of  
243  $1/2^{\circ} \times 2/3^{\circ}$ , covering 1979 to present. Q and  $R_n$  were respectively extracted from the FLX  
244 and RAD collections, meaning that fluxes from inland water are also counted in the pixel  
245 estimate. Q can also be extracted from the LND collection, where only the fluxes coming  
246 from land are counted. For consistency with the other reanalyses estimates used here the  
247 FLX fluxes are included.

### 248 **2.2.3. NCEP-DOE reanalysis (R-2) [NCEP-DOE, NCE]**

249 The National Centers for Environmental Prediction-Department of Energy (NCEP-  
250 DOE) Reanalysis 2 is an improved version of the NCEP-National Center for Atmospheric  
251 research (NCEP-NCAR) Reanalysis I model [Kalnay *et al.*, 1996] that fixed errors and  
252 updated parameterizations of physical processes [Kanamitsu *et al.*, 2002]. Unlike the  
253 NCEP/NCAR reanalysis, NCEP/DOE reanalysis utilizes pentad mean observed precipi-  
254 tation to correct model precipitation in driving the soil model, which made the evolution

---

Science and Technology Center, City

255 of soil moisture more realistic [Lu *et al.*, 2007]. Users of the NCEP reanalysis are warned  
256 that variables such as heat fluxes, humidity, or surface temperature should be interpreted  
257 with caution, as there are no assimilated observations to directly affect these variables.  
258 NCEP-DOE Reanalysis 2 fluxes were provided by the NOAA/OAR/ESRL PSD, Boulder,  
259 Colorado, USA, as daily averages in  $W m^{-2}$  at a resolution of  $\sim 2.0^\circ \times 2.0^\circ$  (T62 Gaussian  
260 grid, 192x94), and are available from 1979.

### 2.3. Off-line models

#### 261 2.3.1. GSWP-2 modeling exercise [GSWP-MMA, gsw]

262 GSWP is an international modeling research activity with the main goal of producing  
263 global datasets of soil moisture, other state variables, and related hydrological quantities  
264 using state-of-the-art land surface models. In the second phase of the project (GSWP-  
265 2)[Dirmeyer *et al.*, 2006], 15 land surface models driven in off-line mode using global  
266 meteorological forcing inputs produced daily land fluxes and related surface variables  
267 for 10 years (1986-1995) at a resolution of  $1^\circ \times 1^\circ$ . The model forcing, vegetation, and soil  
268 cover were primarily extracted from the ISLSCP-II initiative, though work was undertaken  
269 to hybridize the reanalyses data with observational data in order to remove systematic  
270 errors [Zhao and Dirmeyer, 2003]. The flux estimates compared here are the multi-model  
271 ensemble monthly averages in  $W m^{-2}$  publically available at the GSWP web site. In Guo  
272 and Dirmeyer [2006], the GSWP-2 multi-model analysis resulting from a simple average  
273 across the individual models gave the best overall results when evaluating the modeled  
274 soil moisture outputs. This model ensemble is described as an analog to the atmospheric

---

College of New York, New York, USA.

reanalyses, and judged as the best approach to combine the models, compared with more sophisticated combinations, in the absence of calibration data [Dirmeyer *et al.*, 2006].

### 2.3.2. GLDAS [GLDAS-Noah/CLM/Mosaic, NOAA, CLM, MOS]

The Global Land Data Assimilation System (GLDAS) [Rodell *et al.*, 2004] drives multiple off-line land surface models, integrating a large quantity of observation based data enabled by the Land Information System (LIS) [Kumar *et al.*, 2006]. Currently, GLDAS drives four land surface models (Mosaic, Noah, the Community Land Model (CLM), and the Variable Infiltration Capacity (VIC)), forcing them with satellite derived precipitation and radiation data and atmospheric analysis model outputs. For the inter-comparison the  $1^\circ \times 1^\circ$  monthly averages in  $W m^{-2}$  from Noah (version 2.7), CLM (version 2.0) and Mosaic were downloaded. The VIC outputs were not included in this analysis as it was run in "water balance mode", without fully solving the surface energy balance, meaning that  $R_n$  was not available. The radiative downward forcing for 1993 comes from the ERA-15 reanalysis, but for 1994-1995 from the NCEP/NCAR reanalysis R1, both bias corrected with GEWEX-SRB [Berg *et al.*, 2003].

## 2.4. Auxiliary products

### 2.4.1. Precipitation

The Global Precipitation Climatology Project (GPCP) merges rain gauges, satellite geostationary and low-orbit infrared, passive microwave, and sounding observations to estimate monthly rainfall on a  $1^\circ \times 1^\circ$  global grid from 1979 to the present [Adler *et al.*,

---

<sup>6</sup>European Center for Medium-Range



294 2003]. Monthly averaged precipitation amount in  $cm\ month^{-1}$  (version 2.1) is used in the  
295 analysis. These estimates are likely to be different from some of the precipitation gener-  
296 ated by the atmospheric reanalyses or prescribed to the off-line models, and most of the  
297 satellite-based products do not use precipitation as an observational input. Consequently,  
298 the GPCP estimates will only be used to give an approximated idea of the different pre-  
299 cipitation regimes, not to compare evaporation/precipitation regimes across the different  
300 products.

#### 301 **2.4.2. Snow**

302 A snow mask is obtained from a combination of National Snow and Ice Data Center  
303 (NSIDC) data. The snow mask is derived from the NSIDC Northern Hemisphere EASE-  
304 Grid Weekly Snow Cover and Sea Ice Extent Version 3 [Armstrong and Brodzik, 2005]  
305 and the weekly Southern Hemisphere snow flag stored by ISCCP (derived from NSIDC  
306 data).

#### 307 **2.4.3. Surface water**

308 A globally applicable remote-sensing technique employing a suite of complementary  
309 satellite observations has been developed to estimate spatial and temporal dynamics of  
310 surface water extent [Prigent *et al.*, 2001b; Papa *et al.*, 2010]. This dataset has been gen-  
311 erated from several satellite instrument types: passive microwave (SSM/I), scatterometer  
312 (ERS), and visible and near-IR (AVHRR). It will be used here to identify regions with a  
313 likely presence of inland water.

#### 314 **2.4.4. Vegetation**

---

Weather Forecasts, Reading, UK.

315 The vegetation and land use dataset of *Matthews* [1983] will be used to classify the flux  
316 estimates into 10 vegetation classes. The *Matthews* [1983] classification distinguishes 30  
317 classes of natural vegetation, and is associated to a land use dataset that distinguishes 5  
318 levels of cultivation intensity. The version used here is a simplified classification compiled  
319 in *Prigent et al.* [2001a], where the original classes are re-grouped into 9 natural vegetation  
320 classes and one cultivation class. This classification is likely to differ from the land cover  
321 masks employed in some of the data products, and it will be used only for an approximate  
322 separation of the estimates into vegetation types.

#### 323 **2.4.5. Basins**

324 The template of the major river basins from TRIP (Total Runoff Integrating Pathways)  
325 [*Oki and Su*, 1998] is adopted in this study to delineate the spatial extension of a group  
326 of selected basins. The selected basins correspond to the rivers Amazon, Mississippi and  
327 Parana (America); Danube, Volga and Yantgze (Eurasia); Nile, Niger and Congo (Africa);  
328 and Murray (Australia).

### **3. Methodology**

329 To make the inter-comparison possible the different products have been aggregated to a  
330 common spatial and temporal resolution. First, the spatial resolution of the products has  
331 been downgraded to the  $2.5^{\circ} \times 2.5^{\circ}$  resolution of the coarser product (PRU) by spatially  
332 averaging the original estimates. Next, the products are space-matched, i.e., only pixels  
333 having fluxes from all products are retained. Finally, the products are time matched: only

---

<sup>7</sup>Atmospheric Research, Pittsford,

334 pixels having fluxes for all months, years and products are kept. This guarantees that  
 335 differences in the statistics are not due to different spatial coverage or time period. After  
 336 these operations, for each month  $\sim 2600$  pixels at the  $2.5^\circ \times 2.5^\circ$  resolution are compared.  
 337 This represents  $\sim 70\%$  of the total land surface, with most of the missing pixels over  
 338 Greenland and Northern Africa. This implies that the reported globally averaged fluxes  
 339 will not be truly global (although for simplicity they will be referred as global).

340 During the analysis, estimates of  $Q_{le}$ ,  $Q_h$ ,  $R_n$ , and the evaporative fraction (EF) are  
 341 compared. Strictly speaking EF is defined as  $Q_{le} / (Q_{le} + Q_h)$ , but the ratio  $Q_{le} / R_n$   
 342 is used here as only  $Q_{le}$  and  $R_n$  is reported by some of the products. Assuming the  
 343 surface energy balances, i.e.,  $R_n = Q_{le} + Q_h + Q_g$ , where  $Q_g$  is the ground heat flux,  
 344 the difference between both expressions depends on the magnitude of  $Q_g$ . At monthly  
 345 time steps  $Q_g$  is generally a small fraction of  $R_n$ . However,  $Q_g$  estimates as large as  $\sim 15$   
 346  $W m^{-2}$  are reported at some winter locations by some of the products considered here.  
 347 This implies that the EF presented here may differ from the EF reported elsewhere for  
 348 some of the products compared. Notice also that when  $Q_{le}$  and  $R_n$  are very small and/or  
 349 when they take negative values (e.g., for winter conditions in some regions) the  $Q_{le} / R_n$   
 350 ratio can be well outside the 0 to 1 interval. For those situations the EF will not be  
 351 reported.

352 When spatial and/or time averages are required for  $Q_{le}$ ,  $Q_h$ , and  $R_n$ , they are estimated  
 353 by calculating the mean. For the EF, the spatial and/or time  $Q_{le}$  and  $R_n$  means are first  
 354 calculated, and their ratio given as an estimate of the EF average. For those products  
 355 where  $Q_h$  is not directly provided (UCB, UMD, PRU),  $Q_h$  is derived by assuming the

Vermont, USA.

356 surface energy balance. For PRU an estimate of  $Q_g$  is given and is included in the energy  
357 balance. For UCB and UMD  $Q_g$  is not given and assumed here to be zero at the monthly  
358 scale. Differences in  $Q_h$  between UCB and UMD and the other products could then be  
359 related to the fact a zero  $Q_g$  is assumed here for UCB and UMD.

360 For MPI-BGC and PA-OBS an estimate of  $R_n$  is not given. Contrary to some of  
361 the other satellite-based products where the model partitions  $R_n$  into its different flux  
362 components, MPI-BGC  $Q_{le}$  and  $Q_h$  come from a global upscaling of EC measurements  
363 that does not require a  $R_n$  product. Here the sum  $Q_{le} + Q_h$  is used as an approximation  
364 of the MPI-BGC  $R_n$ . For PA-OBS the situation is different. PA-OBS uses the ISCCP  $R_n$   
365 product as an input, but the empirical model is adjusted to reproduce the GSWP  $Q_{le}$  and  
366  $Q_h$ . This means that on average the PA-OBS  $Q$  are consistent with the GSWP  $R_n$ , and  
367 the ISCCP  $R_n$  cannot be used to analyze the partitioning of the fluxes (see *Jiménez et al.*  
368 [2009] for more details). As for MPI-BGC, the sum  $Q_{le} + Q_h$  is used as an approximation  
369 of PA-OBS  $R_n$ . Some of the differences in  $R_n$  between MPI-BGC and PA-OBS and the  
370 other products can be related to this approximation.

371 Most of the  $Q_{le}$  estimates were available as monthly averages expressed in  $W m^{-2}$  and  
372 no time-averaging and/or unit-conversion were required. The exceptions were UCB and  
373 PRU, where  $Q_{le}$  was converted from water depths to  $W m^{-2}$  multiplying by the latent  
374 heat of vaporization (constant value of  $2.45 MJ kg^{-1}$ ) and dividing by the respective time  
375 integration (month and day, respectively). The PRU were further time averaged to get the  
376 monthly means. All products were also annually averaged for 1993 and 1994 by calculating

---

<sup>8</sup>Center for Ocean-Land-Atmosphere

377 for each geographical pixel the average of the 12 monthly means. For 1995 the products  
378 UCB and UMD do not have fluxes for November and December (although a climatological  
379 value was used to make the product aggregation for these 2 months possible), and the

---

Studies, Calverton, Maryland, USA.

<sup>9</sup>Environmental Change Institute, School  
of Geography and the Environment, Oxford  
University, Oxford, UK.

<sup>10</sup>Max Planck Institute for  
Biogeochemistry, Jena, Germany.

<sup>11</sup>Scripps Institution of Oceanography,  
University of California, San Diego, USA.

<sup>12</sup>Global Modeling and Assimilation  
Office, NASA Goddard Space Flight  
Center, Greenbelt, Maryland, USA.

<sup>13</sup>Hydrological Sciences Branch, NASA  
Goddard Space Flight Center, Greenbelt,  
Maryland, USA.

<sup>14</sup>Department of Integrative Biology,  
University of California, Berkeley, USA.

<sup>15</sup>Department of Geological Science,  
University of Texas at Austin, Austin, USA.

380 annual means are not calculated. When plotting monthly time series, the last two months  
381 of the year will be left empty for these two products.

382 During the analysis, an all-product ensemble mean and standard deviation will be dis-  
383 played together with the individual fluxes in most of the figures. Notice that the objective  
384 of this is to highlight the dispersion in the fluxes, not to suggest that an all-product aver-  
385 age is a possible outcome of the inter-comparison exercise. The term spread will be used  
386 in the text to refer to the difference between the maximum and minimum estimate in the  
387 all-product ensemble for a given spatial and/or time average.

## 4. Analysis

### 4.1. Comparing annual fluxes

#### 388 4.1.1. Global fluxes

389 The 1994 global annual means of  $Q_{le}$ ,  $Q_h$ , and  $R_n$  for the different products are plotted  
390 in Figure 1 (left panel). The panel plotting global  $Q_{le}$  versus  $R_n$  shows a spread of  
391  $\sim 20 W m^{-2}$  ( $\sim 15 W m^{-2}$  if the NCEP-DOE estimate is excluded) for  $Q_{le}$  and  $R_n$ , and  
392 a larger spread for  $Q_h$ . The  $Q_{le}$  ensemble mean and standard deviation of the annual  
393 means are  $\sim 45 W m^{-2}$  and  $\sim 6 W m^{-2}$ , respectively. As expected, there is some tendency  
394 of higher  $Q_{le}$  for larger  $R_n$ , but with a much larger scatter than if all products were  
395 similarly partitioning  $R_n$ . The reanalyses have the largest  $Q_{le}$  averages (apart from the  
396 satellite-based product UCB), but the same does not apply to the  $Q_h$  averages. From the  
397 off-line models, GLDAS-Noah and GLDAS-CLM have more similar  $Q_{le}$  and  $Q_h$  averages  
398 (compared with GLDAS-Mosaic), coinciding also with more similar  $R_n$ . GSWP-MMA,  
399 PA-OBS, and MPI-BGC have closer fluxes, compared with the differences with the other  
400 products. This is expected for GSWP-MMA and PA-OBS, as PA-OBS fluxes are derived

401 from an empirical model calibrated with GSWP-MMA fluxes. Similar differences are  
 402 observed for the 1993 annual means (not shown).

403 The 1994 annual  $Q_{le}$  from the different products is plotted in Figure 2 (see Figures S1  
 404 to S3 in the auxiliary material for  $Q_h$ ,  $R_n$ , and EF). In broad terms, the expected spatial  
 405 structures related to the main climate regimes and topographical features are present in  
 406 all products. Nevertheless, the absolute values of the fluxes can be quite different from  
 407 one product to the other. In terms of spatial structures, MERRA  $Q_{le}$  and  $Q_h$  over the  
 408 Tropics seem different compared to the others, with a sharp flux gradient around  $10^\circ\text{S}$ . To  
 409 highlight the differences, the 1994 all-product ensemble  $Q_{le}$ ,  $Q_h$ , and  $R_n$  annual average  
 410 and the absolute and relative standard deviation (from the 12 products annual means and  
 411 normalized by the all-product ensemble average) are given in Figure 3. Globally, there is  
 412 more variability in the derived  $Q_h$  than  $Q_{le}$ . Compared with  $Q_{le}$ , the absolute variability  
 413 in  $R_n$  is larger, but as the absolute  $R_n$  values are in general larger than the values for  $Q_{le}$ ,  
 414 this results in a smaller relative standard deviation for  $R_n$  (i.e., in relative terms there is  
 415 less variability in  $R_n$ ). This is expected as some products share common downward or  
 416 net radiative fluxes. In general the largest relative variability is observed in those regions  
 417 where the fluxes are smaller (e.g., over deserts and mountainous regions for  $Q_{le}$ ). Similar  
 418 statistics are found for 1993 (not shown).

#### 419 4.1.2. Precipitation regimes

420 Figure 1 (center and right panels) show the annual fluxes for two different precipitation  
 421 regimes (using the GPCP estimates): a first one representing regions with high precipita-  
 422 tion ( $P > 1700 \text{ mm year}^{-1}$ ), and a second one representative of drier ecosystems ( $500 >$   
 423  $P > 1000 \text{ mm year}^{-1}$ ). For the averages when precipitation is high, most of the products

424 have a more constant  $Q_{le}$  to  $R_n$  ratio (i.e., a closer flux partitioning) compared with  
425 the global averages, although NCEP-DOE, UMD, and PRU deviate more from the ratio  
426 shown by the other products. Notice that even if there is a larger spread of absolute  
427 annual  $Q_{le}$  averages for the high precipitation regime, Figure 3 shows that in relative  
428 terms the observed variability for some of these regions (e.g, the Amazonia) is compara-  
429 ble to the variability for some more drier regions (e.g. some southern regions in North  
430 America). For the drier regions,  $Q_{le}$ ,  $Q_h$ , and  $R_n$  are smaller than for the wetter regions,  
431 as expected from the precipitation regime and radiation available at these regions, with  
432 the fluxes scattered in ranges similar to the scatter for the global averages.

433 The UCB and UMD products can be used to illustrate possible factors responsible for  
434 flux differences. For instance, for the high precipitation averages, UCB and UMD  $Q_{le}$   
435 differ by  $\sim 25 \text{ W m}^{-2}$ . UCB and UMD use the same datasets for  $R_n$  and near-surface  
436 air temperature. However, soil moisture is characterized differently (water vapor pressure  
437 for UCB, diurnal air temperature range for UMD), and the models are very different  
438 (Priestley-Taylor formulation versus an empirical model). Furthermore, the UCB model  
439 includes a simple parameterization for evaporation from intercepted rain, which may be  
440 of importance for the regions with high canopy density [e.g., Wang *et al.*, 2007a], while  
441 it is not clear how the UMD model calibrated on Southern Great Plains EBBR fluxes  
442 accounts for the interception in high density canopy areas. All these differences in model  
443 and inputs may contribute to the  $Q_{le}$  differences.

#### 444 4.1.3. Snow-covered regions

445 To further characterize the fluxes in regions of large variability, an example showing  
446 the annual averages of  $Q_{le}$  as a function of  $R_n$  for snow-covered regions in Dec-Jan-Feb



447 (selected by using the NSIDC snow cover mask) and for the same regions in Jul-Aug-Sep  
448 is given in Figure 4. Snow-covered regions are difficult to characterize, both from models  
449 and observations [e.g., *Boone et al.*, 2004; *Cordisco et al.*, 2006; *Rutter et al.*, 2009]. A  
450 large spread (relative to their absolute values) both for  $Q_{le}$  and  $R_n$  can be observed in  
451 winter. In the absence of snow, the summer fluxes show expected larger values, with  
452 relatively close  $Q_{le}$  to  $R_n$  ratios among the products, apart from PRU, which has the  
453 smaller  $Q_{le}$  for the largest  $R_n$ .

#### 454 4.1.4. Impact of data aggregation

455 The aggregation to a common spatial and temporal resolution of the different products  
456 can have an impact on the inter-comparison. To see the impact of the grid selection, the  
457 global statistics were re-calculated after re-gridding all products onto the finest product  
458 grid (PA-OBS, an equal area grid of  $\sim 770 \text{ km}^2$  with a lat-lon box of  $\sim 0.25^\circ \times 0.25^\circ$  at the  
459 equator). A simple nearest-neighbor technique was used for the re-gridding in order to  
460 keep as much as possible the original spatial structures. Figure 5 (top panels) shows the  
461 global differences between the products aggregated into the fine grid. Comparison with  
462 similar plots in Figure 1 (estimates aggregated into the  $2.5^\circ \times 2.5^\circ$ ) show some differences  
463 (e.g., the global  $Q_{le}$  ensemble mean differ by  $\sim 2 \text{ W m}^{-2}$ ), but the relative differences  
464 between individual products are very similar. Another issue is the use of different land  
465 masks. For instance, even if only common land surface pixels are compared, for pixels  
466 with a mixture of land and water bodies the reanalyses or off-line model fluxes could  
467 have been estimated with different land/water partitions. Another problem is that the  
468 observational data could already have been integrating the land/water contributions (e.g.,  
469 if land and water bodies are within the satellite footprint). This is likely to have a direct

470 effect on the satellite-based products that depend more directly on the observational data.  
471 To have some idea about how this might be impacting the differences, the surface water  
472 product was used to select pixels that are unlikely to have a presence of inland or coastal  
473 water. In principle, those are pixels where potential differences related to these issues can  
474 be excluded. Figure 5 (bottom panels) shows the new differences. A comparison with  
475 Figure 1 shows that although the product averages change (expected as the geographical  
476 coverage has changed), the relative differences between products remain quite similar.  
477 These examples suggest that although the aggregation into a common spatial and temporal  
478 resolution has an effect on the analysis, it is unlikely to be responsible for a large part of  
479 the observed differences.

## 4.2. Comparing seasonal fluxes

### 480 4.2.1. Monthly fluxes

481 An example of monthly  $Q_{le}$  and  $R_n$  (August 1994) for the different products is given in  
482 Figures 6 and 7 (see Figures S4 to S10 for  $Q_{le}$ ,  $Q_h$ ,  $R_n$ , and EF for February and August  
483 1994 in the auxiliary material). As with the annual averages, the main geographical  
484 structures related to the main climatic regimes and geographical features are in general  
485 present in all products. Nevertheless, the differences in the  $Q_{le}$  absolute values can be  
486 large, e.g., the differences between PA-OBS and PRU for Northern Europe, or between  
487 ERA-INT and MERRA in South America. In the latter case, some of the differences  
488 can be traced back to the MERRA precipitation, which differ from standard gauge- and  
489 satellite-based products, and to details in the interception formulation in MERRA. Re-  
490 running the MERRA integrations in off-line mode with observation-corrected precipitation  
491 narrows the  $Q_{le}$  differences considerably (not shown). The  $R_n$  maps seem to be in better

492 agreement, but large differences can also be observed (e.g., compare PA-OBS and GLDAS-  
493 Mosaic). Large differences in the partitioning of the fluxes are also evident in the EF maps  
494 (e.g., see Figure S10 in the auxiliary material). Maps of the monthly mean  $Q_{le}$  and  
495  $R_n$  differences with the all-product ensemble average for the same month are given in  
496 Figures 8 and 9. Large regions with  $Q_{le}$  and  $R_n$  differences (with respect to the ensemble  
497 mean) larger than  $30 W m^{-2}$  can be observed for some products.

498 To summarize the monthly mean statistics, Tables 2 and 3 report the mean difference  
499 and the root mean square (RMS) difference of the global 1994 product-to-product differ-  
500 ences for  $Q_{le}$  and  $R_n$ , respectively. The correlations between the different products are  
501 also given. The statistics are computed by including for each product the monthly fluxes  
502 for all the pixels and months, meaning that the correlations reflect both the spatial and  
503 temporal variations between the products. In general, the correlations for  $Q_{le}$  are high  
504 (values between 0.72 and 0.95). Some of the lowest correlations relate to the NCEP-DOE  
505 and MERRA reanalyses, which can be explained by some of the observed spatial struc-  
506 tures. If the products are divided into satellite-based products, reanalyses, and off-line  
507 models, Table 2 suggests that the reanalyses  $Q_{le}$  presents the largest RMS difference  
508 among them (a high of 30.7 for the pairs NCEP-DOE and GSWP-MMA, and MERRA  
509 and GLDAS-CLM). Nevertheless, some of the mean differences for the satellite-based  
510 products are larger than the mean differences for the reanalyses (a high of 12.9 for the  
511 pair UCB and MPI-BGC). Table S3 (Section S4.2) shows the same statistics for  $R_n$ , where  
512 the correlations are in generally higher. This is expected as some of the radiative forcings  
513 (e.g., the GLDAS off-line models, or UCB and UMD) are common. Nevertheless, some  
514 significant differences between some products are observed (e.g., between GSWP-MMA

515 and UCB, or PRU and GLDAS-Mosaic). It should be clear that such differences in  $R_n$   
516 limit a possible agreement between estimates of  $Q$ . At the same time, the  $R_n$  differences  
517 cannot be used to completely explain  $Q$  differences, since variation in the partitioning of  
518 the fluxes was observed in Figure 1.

#### 519 4.2.2. Annual cycles

520 The 1994  $Q_{le}$ ,  $R_n$ , and EF global annual cycles are displayed in Figure 10. The  $Q_{le}$   
521 annual cycles have close shapes, with all products having maximum global  $Q_{le}$  in July,  
522 illustrating the dominance of the Northern Hemisphere land areas. At the cycle maximum,  
523 there is a spread of  $\sim 25 W m^{-2}$ , with an ensemble mean and standard deviation of  $\sim 60$   
524 and  $\sim 10 W m^{-2}$ , respectively. For  $R_n$  the annual cycles peak between June and August,  
525 depending on the product. Some of the products having relatively small amplitude in the  
526  $R_n$  cycle also have small amplitudes in the  $Q_{le}$  cycle (e.g., GSWP-MMA), but this is not  
527 always the case (e.g., PRU, with one of the largest  $R_n$  and smaller  $Q_{le}$  cycles). For EF  
528 the annual cycles are more different from one product to another, though all of them peak  
529 between July and September. For the month of highest  $Q_{le}$  (July), the EF vary between  
530  $\sim 0.4$  to  $\sim 0.7$ , suggesting significant differences in the way the different models partition  
531 the fluxes. Close annual cycles are found for 1993 (not shown). The more distinctive  
532 products are NCEP-DOE and PRU with EF from most months outside the envelope  
533 defined by the all-product ensemble mean  $\pm$  one standard deviation.

#### 534 4.2.3. Zonal means

535 Zonal means of  $Q_{le}$  and  $R_n$ , and EF for the months of February and August 1994 can  
536 be found in Figure 11. As expected, the seasonal changes in the latitudes of maximum  
537  $R_n$  are reflected in the seasonal changes of  $Q_{le}$  with latitude. Although the differences

in absolute values can be large between products (e.g., at the latitudes of largest  $Q_{le}$  in February, a  $Q_{le}$  spread of  $\sim 40 W m^{-2}$ , with a ensemble mean and standard deviation of  $\sim 100 W m^{-2}$  and  $15 W m^{-2}$ , respectively), in broad terms the shapes of the latitudinal distributions seem in general to be consistent from one product to another (e.g., see the triple-peak shape in the August zonal means). The zonal means for August 1993 show similar shapes (not shown).

#### 4.2.4. Monthly anomalies

The global annual correlations are studied further by removing the seasonal component from the flux time series. For each pixel and month the inter-annual mean fluxes are first calculated by averaging the three (1993-1994-1995) monthly values (apart from UCB and UMD November and December, where only the two 1993 and 1994 values are used). The inter-annual mean flux is then subtracted from the original monthly mean fluxes to obtain the monthly anomalies, referred to here as the deseasonalized fluxes. Table 4 gives a summary of the original, inter-annual, and deseasonalized  $Q_{le}$ ,  $Q_h$ , and  $R_n$  global correlations for 1994. The correlations are calculated by first adding together the correlations of each product with all the other products, followed by dividing by the number of products (i.e., by doing a product-average). Table 4 shows that the inter-annual fluxes correlate slightly higher (0.89 to 0.93 for  $Q_{le}$ ) than the original fluxes (0.86 to 0.91), and much higher than the deseasonalized fluxes (0.12 to 0.45). This confirms that the large seasonal variability of the fluxes (e.g., see Figure 10) is partly responsible for the high correlations between the products. The fact that some products are not completely independent can also be seen in the individual product-to-product correlations for the deseasonalized fluxes. For instance, UCB and UMD models share a large number of forcings, and the  $Q_{le}$  correlation is the

561 highest of all products (0.83). The same applies to the GLDAS-Noah, GLDAS-CLM, and  
 562 GLDAS-Mosaic models, forced with the same datasets, exhibiting higher correlations than  
 563 other products (0.70 to 0.79). Table 4 also shows that the lowest correlations are for the  
 564 MPI-BGC deseasonalized fluxes (0.12 for  $Q_{le}$ ), even if the inter-annual fluxes agree well  
 565 with the other products (0.91). One might speculate that the use of the in-situ datasets  
 566 (e.g, the EC measurements and GPCC precipitation) by MPI-BGC (in contrast to some  
 567 of the other products using more satellite based forcings) may be a factor explaining the  
 568 low deseasonalized correlations, but this cannot be further tested here.

### 4.3. Comparing fluxes for different vegetation classes

#### 569 4.3.1. Annual differences

570 The vegetation classes are displayed in Figure 12. The class averaged 1994  $Q_{le}$  and  
 571  $R_n$  annual means for the different classes are presented in Figure 13. The class averaged  
 572 annual precipitation amount (as estimated from the GPCP data) is also given for each  
 573 class. The largest spread in  $Q_{le}$  are observed for the the rain forest ( $\sim 35 W m^{-2}$ , with an  
 574 ensemble mean and standard deviation of  $\sim 98$  and  $25 W m^{-2}$ ), and for  $R_n$  in the desert  
 575 ( $\sim 60 W m^{-2}$ , with an ensemble mean and standard deviation of  $\sim 75$  and  $40 W m^{-2}$ ).  
 576 Close results are found for 1993 (nor shown).

577 The large  $Q_{le}$  differences in the rain forest (compared with the other vegetation types)  
 578 may indicate larger observational or modeling difficulties for these regions. Conventional  
 579 interception-measurement in tropical rain forest sites (e.g, see reported 8% to 40% of  
 580 total annual precipitation from a compilation in *Czikowsky and Fitzjarrald* [2009]) suggest  
 581 that canopy evaporation from intercepted rain can be an important component of  $Q_{le}$ .  
 582 Therefore, differences in how interception is modeled may have a larger importance in this

583 region, contributing to some of the observed differences. The reanalyses and off-line models  
584 compared here have schemes that account for rain interception, but of the satellite-based  
585 products only UMD explicitly accounts for evaporation of intercepted water. Nevertheless,  
586 the large differences could also be related to larger absolute fluxes, compared with other  
587 regions. If the differences between the products are normalized by the average flux for  
588 each product and class, the normalized mean and RMS differences for the rain forest  
589 are now comparable to other classes. This is illustrated in Table 5. For instance, the  
590 normalized RMS difference for the rain forest takes values between 0.21 and 0.37, while a  
591 larger difference between 0.33 and 0.50 is found for the cultivated areas.

#### 592 4.3.2. Seasonal correlations

593 The seasonal correlations between  $Q_{le}$  and  $R_n$  for the different products and vegetation  
594 classes are displayed in Table 6 for Dec-Jan-Feb and Jul-Aug-Sep 1994. To have a well  
595 defined seasonal cycle, the correlations are calculated only for the classes in Tropical and  
596 Northern hemisphere regions (pixels with latitude  $< 20^\circ\text{S}$  are removed). In general, the  
597 correlations are higher for the satellite-based products, compared with the reanalyses and  
598 off-line models. This may be related to a more direct dependence of  $Q_{le}$  on  $R_n$  in the  
599 simpler models used by the satellite-based products (in contrast to the more complex  
600 parameterizations used in the reanalyses and off-line models). For most of the classes  
601 there is consistency in how the correlations for the different products change from winter  
602 to summer. For instance, for cultivation, grassland and shrubland there is a clear change  
603 in correlations between the winter-dry period (e.g., 0.70 to 0.93 for cultivation) and the  
604 summer-wet (0.42 to 0.81), with all products suggesting a larger control of  $Q_{le}$  by  $R_n$   
605 for the winter-dry conditions. For the evergreen, deciduous forest, and woodlands, the

606 correlation changes between winter and summer are smaller than before, with less variation  
607 in the correlations for the satellite-based products than for the reanalyses and off-line  
608 models. For the rain forest, all products but NCEP-DOE have smaller correlations for  
609 the winter-wet than for the summer-dry season, although the correlation coefficients and  
610 seasonal difference vary considerably from one product to another (e.g., 0.82 to 0.88  
611 for UCB, 0.05 to 0.54 for GLDAS-CLM). Correlations for only for the Amazonian rain  
612 forest have also been calculated and added to Table 6. Closer correlations between wet  
613 and dry season are observed. Although some satellite-based products have slightly larger  
614 correlations for the wet season (UCB and MPI-BGC), larger correlations are observed  
615 again for the dry season across most of the products. *Hasler and Avissar* [2007] shows  
616 evidence of the opposite: larger correlations for the wet season than for the dry season  
617 from EC measurements at a few Amazon rain forest sites, but it is uncertain whether this  
618 results holds for the whole Amazon rain forest averaged fluxes compared here.

#### 4.4. Comparing fluxes for different river basins

##### 619 4.4.1. Annual differences

620 The geographical location and extent of the 10 selected basins are displayed in Fig-  
621 ure 14. They include some of the major tropical and mid-latitudes river systems. The  
622 basin averaged  $Q_{le}$  and  $R_N$  1994 annual means for the different basins are presented in  
623 Figure 15. Close differences are observed for 1993 (not shown). The basin averaged annual  
624 precipitation amount (as estimated from the GPCP data) is also given for each basin. A  
625 larger relative spread (with respect to the all-product ensemble mean) in the annual  $Q_{le}$   
626 is seen for the Danube, Congo, Volga, and Nile basins. For  $R_N$ , the larger relative spread  
627 is observed for the Yangtze, Danube, Niger and Volga. One could speculate that the large



628 spread in the African basins may be related to difficulties in properly modeling some of the  
629 unique features of these regions (e.g., the West African Monsoon), further aggravated by  
630 a lack of observations (compared with other better characterized regions). For instance,  
631 UMD used EC and EBBR fluxes for the development/validation of its product, but no  
632 measurements over Africa are included; UCB uses EC fluxes from 36 stations, but only  
633 one is located in Africa. The Danube is the highest latitude basin considered, and the  
634 variability may be related to the difficulties in modeling the winter months. In terms of  
635 products, the reanalyses NCEP-DOE, MERRA and ERA-INT have in general the largest  
636 basin averaged  $Q_{le}$ , but this is not followed by the largest basin averaged  $R_n$  (e.g., over  
637 the Congo basin, where they have some of the smallest  $R_n$ ). For the GLDAS off-line  
638 models, GLDAS-Mosaic has more distinct fluxes than GLDAS-CLM and GLDAS-Noah.  
639 For these off-line models a scaling of  $Q_{le}$  as a function of  $R_n$  is apparent for some basins  
640 (e.g., for the Mississippi), but this does not hold for some of the other basins (e.g., the  
641 Danube and Yangtze). From the satellite-based products, the plots again show, as ex-  
642 pected, similar fluxes for PA-OBS and GSWP-MMA. PRU exhibits large  $Q_{le}$  and  $R_n$  for  
643 the basins with the highest rainfall (e.g., Amazon and Mississippi), while for most of the  
644 other basins (e.g., Volga, Murray, Parana, or Danube) it has the smallest average  $Q_{le}$  (not  
645 necessarily related to a small  $R_n$ , as for the Volga and Danube basins).

#### 646 4.4.2. Monthly time series

647 Monthly time series of the basin averaged  $Q_{le}$ ,  $Q_h$ ,  $R_n$ , and EF for the Amazon and  
648 Murray rivers are presented in Figures 16 and 17. Figure 16 is representative of a trop-  
649 ical region with large rainfall and relatively small seasonal and inter-annual variability.  
650 Figure 17 represents a drier mid-latitude region with large seasonal and inter-annual vari-

651 ability. For the Amazon basin, PA-OBS and GSWP-MMA have relatively close  $Q_{le}$ , apart  
652 from the last months in 1995, where an anomaly in the GSWP radiative forcing produced  
653 large  $Q_{le}$ . The PA-OBS model driven by the remote sensing observations modify these  
654 fluxes to more expected values (see *Jiménez et al.* [2009] for more details). UMD and  
655 MPI-BGC  $Q_{le}$  are also close to PA-OBS and GSWP-MMA, while PRU and UCB have  
656 relatively higher fluxes.

657 Large differences in the Amazonian modeled  $Q_{le}$  annual cycle have been reported in  
658 *Werth and Avissar* [2004], where it was suggested that the differences come from the  
659 way the vegetation controls the evapotranspiration in the models. Time series of EC  
660 measurements in the Amazon basin ( see the compilation reported in *Fisher et al.* [2009])  
661 show that the seasonal changes depend on the location and water conditions at each  
662 specific site and year. Large seasonal variations in strongly water limited regions with  
663 long dry seasons are presented in *da Rocha et al.* [2009]. In general, the basin averaged  
664 estimates from the satellite-based products presented here do not show much seasonal  
665 variability, and some of the changes appear to be related to variations in  $R_n$  (the EFs are  
666 relatively constant, in agreement with the relatively high  $Q_{le}$  to  $R_n$  correlations discussed  
667 in Section 4.3). For the reanalyses, ERA-INT has a more constant EF (which can be  
668 explained by the lack of seasonal cycle in its vegetation scheme), while NCEP-DOE and  
669 especially MERRA have more variable fluxes (e.g., MERRA EF changes from  $\sim 0.5$  to  
670  $\sim 1$ ). From the GLDAS off-line models, GLDAS-CLM shows the largest changes in  $Q_{le}$   
671 and  $Q_h$ , with differences of  $\sim 50 W m^{-2}$  between the winter and summer months.

672 For the Murray basin, all products show much more seasonality than for the Ama-  
673 zon basin. Nevertheless, some of the products exhibit large inter-annual variability than

674 others. For instance, reanalyses and off-line models show significant changes in  $Q_{le}$  for  
675 January and December during these three years. Some of the satellite-based products  
676 also follow these changes (e.g PA-OBS and MPI-BGC), while some show more constant  
677 fluxes for these two months (e.g., UCB and UMD, which follow each other closely, or  
678 PRU, with smaller fluxes). Close inspection of the mean  $R_n$  seems to show that some of  
679 these different seasonal values are related to corresponding changes in the  $R_n$  forcing the  
680 products.

681 Time series for the remaining basins are presented in the auxiliary material (Figures  
682 S11 to S18). Not much inter-annual variability for the 3 years analyzed is evident, and in  
683 general all products capture the strong seasonality present in some of the basins.

## 5. Summary and conclusions

684 Land surface heat fluxes are essential components of the energy and water cycle. *In*  
685 *situ* measurements of the turbulent land heat fluxes by tower networks exist, but they  
686 lack global coverage. For global estimation, the alternative is a range of models forced by  
687 global datasets providing information about the physical properties of the surface and/or  
688 atmosphere affecting the land surface fluxes.

689 A global inter-comparison of existing sensible ( $Q_h$ ) and latent ( $Q_{le}$ ) heat fluxes (here  
690 collectively referred as  $Q$ ) datasets for a selected period of time (1993-1995) at monthly  
691 time scales is presented here. The inter-comparison includes a representative sample of  
692 the first emerging global satellite-based flux products and some examples of estimates  
693 produced by reanalyses and off-line forced land surface models (off-line models).

694 The analysis presented here was conducted by comparing the different estimates  $Q_{le}$   
695 and  $Q_h$ , the associated net radiative fluxes ( $R_n$ ), and the evaporative fraction ( $EF = Q_{le}$

696 /  $R_n$ ) after space aggregation of the different products onto a grid of  $2.5^\circ \times 2.5^\circ$  (coarsest  
697 resolution of the products compared). Comparison of the global  $Q_{le}$  annual means shows  
698 a spread of  $\sim 20 \text{ W m}^{-2}$  ( $\sim 15 \text{ W m}^{-2}$  excluding the two products with largest and smallest  
699 fluxes) for an all-product ensemble global mean of  $\sim 45 \text{ W m}^{-2}$ . An approximately similar  
700 spread is observed in the global annual means of  $Q_h$  and  $R_n$  (but for  $R_n$  with an ensemble  
701 mean of  $\sim 90 \text{ W m}^{-2}$ , implying a smaller relative spread). In general, the products  
702 correlate well with one another, but it should be noted that the large seasonal variability  
703 of the fluxes and the fact that some of the products share forcings are to a large extent  
704 responsible for this agreement. Some of the lowest correlations occur with the reanalyses  
705 NCEP-DOE and MERRA. Inspection of their global annual mean charts reveal marked  
706 difference at some regions (relative to the other products) that could explain the lower  
707 correlations.

708 Inspection of the monthly mean flux distributions for selected months shows that in  
709 general main geographical structures related to the principal climatic regimes are present  
710 in all products. Nevertheless, large  $Q_{le}$  and  $Q_h$  differences in the absolute values among  
711 some products are observed. Annual cycles for  $Q_{le}$  peak for all products in July. The  
712 spread in the cycles maximum value is  $\sim 25 \text{ W m}^{-2}$  (with an ensemble mean of  $\sim 60$   
713  $\text{ W m}^{-2}$ ). For  $R_n$ , the annual cycles peak between June and August, depending on the  
714 product. For EF, the annual cycles are more different from one product to another, though  
715 all of them peak between July and September. For the month of highest  $Q_{le}$  (July), the  
716 EF vary between  $\sim 0.4$  to  $\sim 0.7$ , suggesting significant differences in the way the different  
717 models partition the fluxes.

718 The fluxes were spatially averaged for 10 major vegetation classes. The larger  $Q_{le}$   
719 differences were observed for the rain forest, but in relative terms (differences normalized  
720 with the annual class fluxes) the mean difference and root mean square differences were  
721 not the largest, compared with the other classes.  $Q_{le}$  to  $R_n$  seasonal correlations for  
722 winter and summer for the different products and classes were calculated. In general, the  
723 correlations were higher for the satellite-based products, compared with the reanalyses and  
724 off-line models. For most of the classes there is consistency in how the correlations for the  
725 different products change from winter to summer. For instance, for cultivation, grassland  
726 and shrubland there is a clear change in correlations between the winter-dry period (e.g.,  
727 0.70 to 0.93 for cultivation) and the summer-wet (0.42 to 0.81). For the rain forest, all  
728 products but NCEP-DOE have smaller correlations for the winter than for the summer  
729 season, although the correlation coefficients and seasonal difference vary considerably from  
730 one product to another. For most of the products, correlations recalculated just for the  
731 Amazon rain forest showed also a smaller correlation for the wet season than for the dry  
732 season.

733 The fluxes were also spatially averaged for a group of 10 selected basins including some  
734 of the major river systems at tropical and mid-latitudes. With respect to the all-product  
735 ensemble average, a relatively large spread in  $Q_{le}$  was observed for the Danube, Congo,  
736 Volga, and Nile basins. For  $R_n$ , the largest relative spread is observed for the Yangtze,  
737 Danube, Niger and Volga. Monthly time series of basin averaged fluxes were plotted for  
738 the three years considered. The seasonality was in general well captured by all products,  
739 but some large differences were observed for some products and basins in the partitioning

740 of the fluxes. Apart from the Murray basin, not much inter-annual variability was noticed  
741 in these three years.

742 Despite the existence of a large body of work characterizing  $Q_{le}$  and  $Q_h$  from the local  
743 to the regional scale [e.g., *Verstraeten et al.*, 2008; *Kalma et al.*, 2008], the extension to  
744 the global scale requires simplified formulations that are adapted to the existing global  
745 datasets and are also robust in the face of the data uncertainties. This inter-comparison  
746 highlights the difficulties of producing such global estimates. Some of the satellite-based  
747 products are first versions, and improvements in the analysed products are already on their  
748 way (e.g., improved UMD estimates [*Wang et al.*, 2010a]), which should result in more  
749 consistent fluxes. Nevertheless, the choice of formulation and forcing datasets will always  
750 have an effect on the estimated fluxes. For instance, choosing ISCCP or GEWEX-SRB as  
751 radiative forcing will immediately have an impact on the fluxes produced. Concerning the  
752 atmospheric reanalyses, important differences in some of the surface physical fields has  
753 also been noted elsewhere [e.g., *Bosilovich et al.*, 2009], and users are typically advised  
754 to use the physical fields (as opposed to the assimilated states) with caution. Regarding  
755 the off-line models, the inter-comparison showed that even when forced with the same  
756 datasets, their parameterizations can have a large effect on the partitioning of the fluxes,  
757 as has already been shown [e.g., *Schlosser and Gao*, 2009]. Nevertheless, an increas-  
758 ing better understanding of the soil-atmosphere-vegetation transfer processes [e.g., *Betts*,  
759 2009; *Seneviratne et al.*, 2010] is driving the improvement of some of the land surface  
760 models considered here [e.g., *Balsamo et al.*, 2009], which should result in a better flux  
761 estimation.

762 This inter-comparison has been made in the framework of the GEWEX LandFlux ac-  
763 tivity, and it is part of a series of inter-comparison exercises coordinated by the LandFlux-  
764 EVAL initiative. This type of exercise will contribute to the objective of identifying and  
765 delivering robust procedures for the production of global land surface heat fluxes.

766 **Acknowledgments.** The LandFlux-Eval initiative acknowledges support by GEWEX.  
767 C. D. Kummerow, as chair of the GEWEX Radiation Panel, is acknowledged for encourag-  
768 ing the LandFlux activity, and contributing to the scientific discussions. The GLDAS data  
769 were acquired as part of the mission of NASA's Earth Science Division and archived and  
770 distributed by the Goddard Earth Sciences (GES) Data and Information Services Center  
771 (DISC) are acknowledged by disseminating the GLDAS data. The Global Modeling and  
772 Assimilation Office (GMAO) and the GES DISC are acknowledged for disseminating the  
773 MERRA data.

## References

- 774 Adler, R., et al., The Version-2 Global Precipitation Climatology Project (GPCP)  
775 Monthly Precipitation Analysis (1970-Present), *J. Hydrol.*, *4*, 1147–1167, 2003.
- 776 Aires, F., C. Prigent, and W. Rossow, Temporal interpolation of global surface skin  
777 temperature diurnal cycle over land under clear and cloudy conditions, *J. Geophys.*  
778 *Res.*, *109*, D04313, 10.1029/2003JD003,527, 2004.
- 779 Anderson, M., and W. Kustas, Thermal Remote Sensing of Drought and Evapotranspi-  
780 ration, *EOS*, *89*, 233–240, 2008.
- 781 Armstrong, R., and M. Brodzik, Northern Hemisphere EASE-Grid weekly snow cover  
782 and sea ice extent version 3, *Tech. rep.*, Boulder, Colorado USA: National Snow and

- 783 Ice Data Center. Digital media., 2005.
- 784 Baldocchi, D., et al., FLUXNET: A new tool to study the temporal and spatial variability  
785 of ecosystem-scale carbon dioxide, water vapor, and energy flux densities, *Bull. Amer.*  
786 *Meteor. Soc.*, *82*, 2415–2434, 2001.
- 787 Balsamo, G., P. Viterbo, A. Beljaars, B. van den Hurk, M. Hirschi, A. K. Betts, and  
788 K. Scipal, A revised hydrology for the ECMWF model: Verification from field site to  
789 terrestrial water storage and impact in the Integrated Forecast System, *J. Hydromet.*,  
790 pp. 623–643, 2009.
- 791 Berg, A., J. Famiglietti, J. Walker, and P. Houser, Impact of bias correction to reanalysis  
792 products on simulations of North American soil moisture and hydrological fluxes, *J.*  
793 *Geophys. Res.*, *108*, 10.1029/2002JD003,334, 2003.
- 794 Betts, A., Land-Surface-Atmosphere Coupling in Observations and Models, *J. Adv. Model.*  
795 *Earth Syst.*, *1*, doi:10.3894/JAMES.2009.1.4, 2009.
- 796 Betts, A., J. Ball, A. Beljaars, M. Miller, and P. A. Viterbo, The land surface-atmosphere  
797 interaction: A review based on observational and global modeling perspectives, *J. Geo-*  
798 *phys. Res.*, *101*, 7209–7226, 1996.
- 799 Betts, A., M. Zhao, P. Dirmeyer, and A. Beljaars, Comparison of ERA40 and NCEP/DOE  
800 near-surface data sets with other ISLSCP-II data sets, *J. Geophys. Res.*, *111*, D22S04  
801 , doi:10.1029/2006JD007,174, 2006.
- 802 Boone, A., et al., The Rhône-Aggregation Land Surface Scheme intercomparison project:  
803 An overview, *J. Clim.*, *17*, 187–208, 2004.
- 804 Boone, A., et al., The AMMA Land Surface Model Intercomparison Project, *Bull. Amer.*  
805 *Meteor. Soc.*, *90*, doi:10.1175/2009BAMS2786.1, 2009.



- 806 Bosilovich, M., NASA's Modern Era Retrospective-analysis for Research and Applications:  
807 Integrating Earth Observations, *EarthZine*, pp. E-Zine article, 2008.
- 808 Bosilovich, M., D. Mocko, J. Roads, and A. Ruane, A Multimodel Analysis for the Coordi-  
809 nated Enhanced Observing Period (CEOP), *J. Hydromet.*, *10*, 11.1175/2009JHM1090.1,  
810 2009.
- 811 Cleugh, H., R. Leuning, Q. Mu, and S. Running, Regional evaporation estimates from  
812 flux tower and MODIS satellite data, *Remote Sens. Environ.*, *106*, 285–304, 2007.
- 813 Cordisco, E., C. Prigent, and F. Aires, Snow characterization at a global scale  
814 with passive microwave satellite observations, *J. Geophys. Res.*, *111*, D19102,  
815 doi:10.1029/2005JD006773, 2006.
- 816 Czikowsky, M., and D. Fitzjarrald, Detecting rainfall interception in an Amazonian rain  
817 forest with eddy flux measurements, *J. Hydrol.*, *377*, 92–105, 2009.
- 818 da Rocha, H., et al., Patterns of water and heat flux across a biome gradient from tropical  
819 forest to savanna in Brazil, *J. Geophys. Res.*, *114*, G00B12, doi:10.1029/2007JG000640,  
820 2009.
- 821 Dirmeyer, P. A., X. Gao, M. Zhao, Z. Guo, T. Oki, and N. Hanasaki, GSWP-2: Mul-  
822 timodel analysis and implications for our perception of the land surface, *Bull. Amer.*  
823 *Meteor. Soc.*, *87*, 1831–1397, 2006.
- 824 Douville, H., P. Viterbo, J.-F. Mahfouf, and A. Beljaars, Evaluation of the optimum  
825 interpolation and nudging techniques for soil moisture analysis using FIFE data, *Month.*  
826 *Weath. Rev.*, *128*, 1733–1756, 2000.
- 827 Drusch, M., D. Vasiljevic, and P. viterbo, ECMWF's global snow analysis: Assessment  
828 and revision based on satellite observations, *J. Appl. Meteor.*, *43*, 1282–1294, 2004.

- 829 Ek, M. B., K. E. Mitchell, Y. Lin, P. Grunmann, E. Rogers, G. Gayno, V. Koren, and  
830 J. D. Tarpley, Implementation of the upgraded Noah land-surface model in the NCEP  
831 operational mesoscale Eta model, *J. Geophys. Res.*, *108 (D22)*, 8851, doi:10.1029/  
832 2002JD003,296, 2003.
- 833 Entin, K. K., A. Robock, K. Y. Vinnikov, V. Zabelin, S. Liu, and A. Namkhai, Evaluation  
834 of Global Soil Wetness Project soil moisture simulations, *J. Meteorol. Soc. Jap*, *77*, 183–  
835 198, 1999.
- 836 Fisher, J. B., K. Tu, and D. D. Baldocchi, Global estimates of the land-atmosphere water  
837 flux based on monthly AVHRR and ISLSCP-II data, validated at 16 FLUXNET sites,  
838 *Remote Sens. Environ.*, *112(3)*, 901–919, 2008.
- 839 Fisher, J. B., et al., The land-atmosphere water flux in the tropics, *Global Change Biology*,  
840 *15*, 2694–2714, 2009.
- 841 Francis, R., et al., The ERS-1 spacecraft and its payload, *ESA Bulletin*, *65*, 27–48, 1991.
- 842 Frison, P. L., and E. Mougin, Monitoring global vegetation dynamics with ERS-1 wind  
843 scatterometer data, *Int. J. Remote Sens.*, *17*, 3201–3218, 1996.
- 844 Gellens-Meulenberghs, F., A. Arboleda, and N. Ghilain, Towards a continuous monitor-  
845 ing of evapotranspiration based on msg data, in *Symposium on Remote Sensing for*  
846 *Environmental Monitoring and Change Detection*, IAHS Series, IUGG, 2007.
- 847 Gobron, N., B. Pinty, O. Ausedat, M. Taberner, O. Faber, F. M. T. Lavergne, M. Ro-  
848 bustelli, and P. Snoeij, Uncertainty estimates for the FAPAR operational products de-  
849 rived from MERIS - Impact of top-of-atmosphere radiance uncertainties and validation  
850 with field data, *Remote Sens. Environ.*, *112*, 1871–1883, 2008.

- 851 Gobron, N., et al., Evaluation FAPAR products for different canopy radiation transfer  
852 regimes: Methodology and results using JRC products derived from SeaWiFS against  
853 ground-based estimations, *J. Geophys. Res.*, *111*, D13110, 10.129/2005JD006511, 2006.
- 854 Grubber, A., and V. Levizzani, Assessment of Global Precipitation Products, *A project*  
855 *of the World Climate Research Programme Global Energy and Water Cycle Experiment*  
856 *(GEWEX) Radiation Panel WCRP-128, WMO/TD-No. 1430*, WCRP, 2008.
- 857 Guo, Z., and P. A. Dirmeyer, Evaluation of the second Global Soil Wetness Project  
858 soil moisture simulations: 1. Intermodel comparison, *J. Geophys. Res.*, *111*, D22S02,  
859 10.129/2006JD07233, 2006.
- 860 Gutman, G. G., On the use of long-term global data of land reflectances and vegetation  
861 indices from the advanced very high resolution radiometer, *J. Geophys. Res.*, *104*, 6241–  
862 6255, 1999.
- 863 Hall, F., E. B. de Colstoun, G. Collatz, D. Landis, P. Dirmeyer, A. Betts, G. Huffman,  
864 L. Bounoua, and B. Meeson, ISLSCP Initiative II global data sets: Surface boundary  
865 conditions and atmospheric forcings for land-atmosphere studies, *J. Geophys. Res.*, *111*,  
866 D22S01, 10.1029/2006JD007366, 2006.
- 867 Hasler, N., and R. Avissar, What Controls Evapotranspiration in the Amazon Basin, *J.*  
868 *Hydromet.*, *8*, 380–395, 2007.
- 869 Henderson-Sellers, A., A. Pitman, P. Love, P. Irannejad, and T. Chen, The project for  
870 Intercomparison of Land Surface parameterization Schemes (PILPS): Phase 2 and 3,  
871 *Bull. Amer. Meteor. Soc.*, *76*, 489–503, 1995.
- 872 Hollinger, J., R. Lo, G. Poe, R. Savage, and J. Pierce, Special Sensor Microwave/Imager  
873 user guide, *Tech. rep.*, Nav. Res. Lab., Washington, D.C, 1987.

- 874 Huete, A., A soil-adjusted vegetation index (SAVI), *Remote Sens. Environ.*, *25*, 295–309,  
875 1998.
- 876 Jiménez, C., C. Prigent, and F. Aires, Toward an estimation of global land sur-  
877 face heat fluxes from multisatellite observations, *J. Geophys. Res.*, *114*, D06305,  
878 doi:10.1029/2008JD011392, 2009.
- 879 Jung, M., M. Reichstein, and A. Bondeau, Towards global empirical upscaling of  
880 FLUXNET eddy covariance observations: validation of a model tree ensemble approach  
881 using a biosphere model, *Biogeosciences Discussion*, *6*, 5271–5304, 2009.
- 882 Kalma, J., T. McVicar, and M. McCabe, Estimating land surface evaporation: a re-  
883 view of methods using remotely sensing surface temperature data, *Surv. Geophys.*, pp.  
884 doi:10.1007/s10712-008-9037-z, 2008.
- 885 Kalnay, E., et al., The NCEP/NCAR 40-year reanalysis project, *Bull. Amer. Meteor.*  
886 *Soc.*, *77*, 437–471, 1996.
- 887 Kanamitsu, M., W. Ebisuzaki, J. Woolen, S. K. Yang, J. J. Hnilo, M. Fiorino, and J. Pot-  
888 ter, The NCEP-DOE AMIP-II reanalysis (R-2), *Bull. Amer. Meteor. Soc.*, *83*, 1631–  
889 1643, 2002.
- 890 Kumar, S. V., et al., Land Information System - An interoperable framework for high  
891 resolution land surface modeling, *Environ. Modeling and Software*, *21*, 1402–1415, 2006.
- 892 Leuning, R., Y. Q. Zhang, A. Rajaud, H. Cleugh, and K. Tu, A simple surface conductance  
893 model to estimate regional evaporation using MODIS leaf area index and the Penman-  
894 Monteith equation, *Water Resour. Res.*, *44*, W10419, doi:10.1029/2007WR006562,  
895 2008.

- 896 Lim, W., and M. Roderick, An Atlas of the Global Water Cycle Based on the IPCC AR4  
897 Climate Models, *Tech. rep.*, published by ANU E Press, Canberra, Australia, ISBN  
898 9781921536892, 2009.
- 899 Los, S., et al., A global 9-year biophysical land-surface data set from NOAA AVHRR  
900 data, *J. Hydromet.*, *1*, 183–199, 2000.
- 901 Lu, C.-H., M. Kanamitsu, J. Roads, W. Ebisuzaki, and K. E. Mitchell, Evaluation of Soil  
902 Moisture in the NCEP-NCAR and NCEP-DOE Global Reanalyses, *J. Hydromet.*, *6*,  
903 391–408, doi: 10.1175/JHM427.1, 2007.
- 904 Matthews, E., Global vegetation and land use: New high-resolution data bases for climate  
905 studies, *J. Clim. Appl. Meteor.*, *22*, 474–487, 1983.
- 906 McCabe, M., and E. Wood, Scale influences on the remote estimation of evapotranspira-  
907 tion using multiple satellite sensors, *Remote Sens. Envir.*, *105*, 271–285, 2006.
- 908 McCabe, M., E. Wood, R. Wójcik, M. Pan, J. Sheffield, H. Gao, and H. Su, Hydrological  
909 consistency using multi-sensor remote sensing data for water and energy cycle studies,  
910 *Remote Sens. Envir.*, *112*, 430–444, 2008.
- 911 Mesinger, F., et al., North American Regional Reanalysis, *Bull. Amer. Meteor. Soc.*, *87*,  
912 343–360, 2006.
- 913 Mu, A., F. Heinsch, M. Zhao, and S. Running, Development of a global evapotranspiration  
914 algorithm based on MODIS and global meteorology data, *Remote Sens. Envir.*, *111*,  
915 519–536, 2007.
- 916 New, M., M. Hulme, and P. Jones, Representing twentieth-century space-time climate  
917 variability. Part I: Development of a 1961–1990 mean monthly terrestrial climatology,  
918 *J. Clim.*, *12*, 829–856, 1999.

- 919 New, M., M. Hulme, and P. Jones, Representing twentieth-century space-time climate  
920 variability. Part II: Development of a 1901-1996 monthly grids of terrestrial surface  
921 climate, *J. Clim.*, *13*, 2217–2238, 2000.
- 922 Nishida, K., R. Nemani, S. Running, and J. Glassy, An operational remote sensing al-  
923 gorithm of land surface evaporation, *J. Geophys. Res.*, *108*, 10.129/2002JD002,062,  
924 2003.
- 925 Oki, T., and Y. C. Su, Design of Total Runoff Integrating Pathways (TRIP): a global  
926 river channel network, *Earth Interactions*, *2*, 1–37, 1998.
- 927 Papa, F., C. Prigent, C. Jimenez, F. Aires, and W. Rossow, Interannual variability  
928 of surface water extent at global scale, 1993-004, *J. Geophys. Res.*, *115*, D12111,  
929 doi:10.1029/2009JD012,674, 2010.
- 930 Papale, D., et al., Towards a standardized processing of Net Ecosystem Exchange mea-  
931 sured with eddy covariance technique: algorithms and uncertainty estimation, *Biogeo-*  
932 *sciences*, *3*, 571–583, 2006.
- 933 Prigent, C., F. Aires, W. Rossow, and E. Matthews, Joint characterization of vegetation  
934 by satellite observations from visible to microwave wavelength: A sensitivity analysis,  
935 *J. Geophys. Res.*, *106*, 20,665–20,685, 2001a.
- 936 Prigent, C., E. Matthews, F. Aires, and W. Rossow, Remote sensing of global wetland  
937 dynamics with multiple satellite data sets, *Geophys. Res. Lett.*, *28*, 4631–4634, 2001b.
- 938 Prigent, C., F. Aires, W. Rossow, and A. Robock, Sensitivity of satellite microwave  
939 and infrared observations to soil moisture at a global scale: Relationship of satellite  
940 observations to in situ soil moisture measurements, *J. Geophys. Res.*, *110*, D07110,  
941 10.1029/2004JD005,087, 2005.

- 942 Prigent, C., F. Aires, and W. Rossow, Land surface microwave emissivities over the globe  
943 for a decade, *Bull. Amer. Meteor. Soc.*, *87*, 1573–1584, 2006.
- 944 Reichstein, M., et al., On the separation of net ecosystem exchange into assimilation  
945 and ecosystem respiration: review and improved algorithm, *Global Change Biology*, *11*,  
946 1424–1439, 2005.
- 947 Rodell, M., et al., The Global Land Data Assimilation System, *Bull. Amer. Meteor. Soc.*,  
948 *85*, 381–394, 2004.
- 949 Rossow, W., and R. Schiffer, Advances in understanding clouds from ISCCP, *Bull. Amer.*  
950 *Meteor. Soc.*, *80*, 2261–2287, 1999.
- 951 Rudolf, B., and U. Schneider, Calculation of gridded precipitation for the global land-  
952 surface using in-situ gauge observations, in *Proceedings of the International Precipitation*  
953 *Working Group. Monterey, California. 25-28 October 2004. ISBN 92-9110-070-6*, pp.  
954 231–247, 2005.
- 955 Rutter, N., et al., Evaluation of forest snow processes models (SnowMIP2), *J. Geophys.*  
956 *Res.*, *114*, D061111, doi:10.1029/2008JD011,063, 2009.
- 957 Schlosser, C., and X. Gao, Assessing Evapotranspiration Estimates from the Global Soil  
958 Wetness Project Phase 2(GSWP-2), *Tech. Rep. 179*, MIT Joint Program on the Science  
959 and Policy of Global Change, 2009.
- 960 Sellers, P., et al., BOREAS in 1997: Experiment overview, scientific results, and future  
961 directions, *J. Geophys. Res.*, *102*, 28,731–28,769, 1997.
- 962 Seneviratne, S. I., T. Corti, E. L. Davin, M. Hirschi, E. B. Jaeger, I. Lehner, B. Orlowsky,  
963 and A. J. Teuling, Investigating soil moisture climate interactions in a changing climate:  
964 A review, *Earth Science Reviews*, *99*, 125–161, 2010.

- 965 Sheffield, J., G. Goteti, and E. Wood, Development of a 50-yr high-resolution global  
966 dataset of meteorological forcings for land surface modeling, *J. Clim.*, *19(13)*, 3088–  
967 3111, 2006.
- 968 Sheffield, J., E. Wood, and F. Munoz-Ariola, Long-term regional estimates of evapotran-  
969 spiration for Mexico based on downscaled ISCCP data, *in revision*, 2009.
- 970 Simmons, A., S. Uppala, D. Dee, and S. Kubayashi, ERA-Interim: New ECMWF reanal-  
971 ysis products from 1989 onwards, *ECMWF Newsletter*, *110*, 25–35, 2006.
- 972 Stackhouse, P., S. Gupta, S. Cox, J. Mikovitz, T. Zhang, and M. Chiacchio, 12-year  
973 surface radiation budget data set, *GEWEX News*, *14*, 10–12, 2004.
- 974 Stöckli, R., D. Lawrence, G.-Y. Niu, K. Oleson, P. Thornton, Z.-L. Yang, and G. Bonan,  
975 Use of FLUXNET in the Community Land Model development, *J. Geophys. Res.*, *113*,  
976 G01025, doi:10.1029/2007JG000,562, 2008.
- 977 Su, H., E. Wood, M. McCabe, and Z. Su, Evaluation of Remotely Sensed Evapotranspi-  
978 ration Over the CEOP EOP-1 Reference Sites, *J. Meteorol. Soc. Jap.*, *85A*, 439–459,  
979 2007.
- 980 Su, Z., The Surface Energy Balance System (SEBS) for estimation of turbulent heat  
981 fluxes, *Hydrol. Earth System Sci.*, *6*, 85–99, 2002.
- 982 van den Hurk, B., P. Viterbo, A. Beljaars, and A. Betts, Offline validation of the ERA40  
983 surface scheme, *Tech. Rep. 295*, ECMWF Technical Memorandum, 2000.
- 984 Vermote, E. F., and N. E. Saleous, An extended AVHRR 8-km NDVI Data Set Compatible  
985 with MODIS and SPOT Vegetation NDVI data, *Int. J. Remote Sens.*, *26*, 4485–5598,  
986 2005.



- 987 Verstraeten, W., F. Veroustraete, and J. Feyen, Assessment of Evapotranspiration and  
988 Soil Moisture Content Across Different Scales of Observation, *Sensors*, *8*, 70–117, 2008.
- 989 Viterbo, P., and A. Beljaars, An improved land surface parameterization scheme in the  
990 ECMWF model and its validation, *J. Clim.*, *8*, 2716–2748, 1995.
- 991 Wang, D., G. Wang, and E. Anagnostou, Evaluation of canopy interception schemes in  
992 land surface models, *J. Hydrol.*, *347(3-4)*, 308–318, 2007a.
- 993 Wang, K., and S. Liang, An Improved Method for Estimating Global Evapotranspiration  
994 Based on Satellite Determination of Surface Net Radiation, Vegetation Index, Temper-  
995 ature, and Soil Moisture, *J. Hydrol.*, *9*, 712–727, 2008.
- 996 Wang, K., P. Wang, Z. Li, M. Cribb, and M. Sparrow, A simple method to estimate  
997 actual evapotranspiration from a combination of net radiation, vegetation index, and  
998 temperature, *J. Geophys. Res.*, *112*, D15107, 10.1029/2006JD008351, 2007b.
- 999 Wang, K., R. E. Dickinson, M. Wild, and S. Liang, Evidence for Decadal Variation in  
1000 Global Terrestrial Evapotranspiration between 1982 and 2002, Part 1: Model Develop-  
1001 ment, *J. Geophys. Res.*, *in press*, doi: 10.1029/2009JD013671, 2010a.
- 1002 Wang, K., R. E. Dickinson, M. Wild, and S. Liang, Evidence for Decadal Variation  
1003 in Global Terrestrial Evapotranspiration between 1982 and 2002, Part 2: Results, *J.*  
1004 *Geophys. Res.*, *in press*, doi: 10.1029/2010JD013847, 2010b.
- 1005 Werth, D., and R. Avissar, The Regional Evapotranspiration of the Amazon, *J. Hy-*  
1006 *dromet.*, *5*, 100–109, 2004.
- 1007 Williams, M., et al., Improving land surface models with fluxnet data, *Biogeosciences*, *6*,  
1008 1341–1359, 2009.

- 1009 Wilson, K., et al., Energy partitioning between latent and sensible heat flux during the  
1010 warm season at FLUXNET sites, *Water Resour. Res.*, *38*, 10.1029/2001WR000989,  
1011 2002.
- 1012 Wright, I., A. Manzi, and H. da Rocha, Surface conductance of Amazonian pasture: model  
1013 application and calibration for canopy climate, *Agric. For. Meteorol.*, *75*, 51–70, 1995.
- 1014 Zhao, M., and P. Dirmeyer, Production and analysis of GSWP-2 near-surface meteorology  
1015 data sets, *Tech. Rep. 159*, Center for Ocean-Land-Atmospheric Studies, 2003.

**Table 1.** Summary of the flux estimates inter-compared. See Section 2 for more details.

	INSTITUTION	$Q_{le}$	$Q_h$	$R_n$	Resolution
<b>SATELLITE-BASED PRODUCTS</b>					
<b>UCB</b>	University of California Berkeley	Physical-biological, Priestley-Taylor, inputs from ISLSCP-II (SRB, CRU, AVHRR)	$R_n - Q_{le}$	SRB	1986-95 monthly 1° x 1°
<b>UMD</b>	University of Maryland	Empirical (linear regression, AmeriFlux $Q_{le}$ ), inputs from ISLSCP-II (SRB, CRU, AVHRR)	$R_n - Q_{le}$	SRB	1986-95 monthly 1° x 1°
<b>PRU</b>	Princeton University	Penman-Monteith, inputs from ISCCP, AVHRR, NCEP/NCAR	$R_n - Q_{le}$	ISCCP-FD	1986-06 daily 2.5° x 2.5°
<b>PAO</b>	Paris Observatory	Empirical (neural networks, GSWP modeled $Q_{le}$ ), inputs from ISCCP, ERS, SSML, AVHRR		$Q_{le} + Q_h$	1992-99 monthly 1/4° x 1/4°
<b>MPI</b>	MPI for Biogeochemistry	Empirical (tree ensemble, FluxNet measured $Q_{le}$ ) inputs from CRU, GPCC, AVHRR.		$Q_{le} + Q_h$	1982-08 monthly 1/2° x 1/2°
<b>REANALYSIS</b>					
<b>MER</b>	NASA-GMAO	MERRA reanalysis, GEOS-5 atmospheric model coupled with Catchment land model			1979- 1-hourly 1/2° x 2/3°
<b>NCE</b>	NCEP/NCAR	NCEP-DOE reanalysis, atmospheric model coupled with OSU land model			1979- 6-hourly 2.5° x 2.5°
<b>ERA</b>	ECMWF	ERA Interim reanalysis, atmospheric model coupled with TESSEL land model			1989-98 6-hourly 3/4° x 3/4°
<b>OFF-LINE LAND SURFACE MODELS</b>					
<b>GSW</b>	GLASS/ISLSCP	Multi-model ensemble, off-line forced with ISLSCP-II		SRB	1986-95 monthly 1° x 1°
<b>NOA</b>	NCAR/OSU/AFWA/HL	Equally off-line forced participating models driven by GLDAS		1993 ERA15 1994/5 NCEP/R1 SRB-bias corrected	1979- 3-hourly 1° x 1°
<b>CLM</b>	NCAR +				
<b>MOS</b>	NASA-GSFC				

**Table 2.** Statistics of the global 1994  $Q_{le}$  monthly mean product differences. The table gives the mean difference (mean) and RMS difference (rmsd) of the monthly means ( $W m^{-2}$ ), and the correlation coefficient ( $r^2$ ) for each pair of products.

	UCB	UMD	PAO	PRU	MPI	NCE	ERA	MER	GSW	NOA	CLM	MOS
UCB	8.41	11.1	14.2	12.9	-6.79	2.95	1.84	12.9	11.5	13.2	6.26	
UMD		2.74	5.78	4.49	-15.2	-5.46	-6.57	4.45	3.06	4.76	-2.15	
PAO			3.04	1.75	-17.9	-8.2	-9.3	1.71	0.32	2.02	-4.89	
PRU				-1.3	-21.0	-11.2	-12.3	-1.33	-2.73	-1.02	-7.93	
MPI					-19.7	-9.95	-11.1	-0.03	-1.43	0.27	-6.64	
NCE						9.74	8.64	19.7	18.3	20.0	13.1	
ERA							-1.1	9.91	8.52	10.2	3.31	
MER								11.0	9.62	11.3	4.42	
GSW									-1.4	0.31	-6.6	
NOA										1.7	-5.21	
CLM											-6.91	
MOS												
	<b>mean</b>											
UCB	17.6	19.6	23.2	21.1	24.3	17.2	24.9	23.1	22.3	28.0	21.6	
UMD		15.5	21.6	17.3	29.8	18.5	30.0	19.2	19.0	27.0	23.0	
PAO			18.0	13.2	28.1	15.9	25.9	12.8	14.6	21.1	19.2	
PRU				15.5	32.4	21.2	27.8	21.3	20.0	22.0	23.3	
MPI					28.5	17.0	25.8	16.1	13.9	18.9	19.9	
NCE						21.8	24.9	28.6	28.0	30.1	25.3	
ERA							23.5	17.0	16.7	22.2	17.2	
MER								26.4	26.3	26.8	24.6	
GSW									12.8	18.3	16.6	
NOA										16.5	14.6	
CLM											19.1	
MOS												
	<b>rmsd</b>											
UCB	0.94	0.93	0.90	0.93	0.85	0.92	0.84	0.89	0.89	0.82	0.88	
UMD		0.90	0.84	0.88	0.81	0.89	0.76	0.87	0.86	0.75	0.85	
PAO			0.89	0.93	0.87	0.93	0.85	0.94	0.91	0.85	0.91	
PRU				0.92	0.83	0.89	0.84	0.84	0.86	0.84	0.86	
MPI					0.89	0.93	0.87	0.90	0.92	0.88	0.91	
NCE						0.89	0.86	0.88	0.88	0.86	0.88	
ERA							0.86	0.93	0.93	0.87	0.92	
MER								0.85	0.85	0.85	0.85	
GSW									0.94	0.89	0.94	
NOA										0.91	0.96	
CLM											0.91	
MOS												
	<b>r<sup>2</sup></b>											

**Table 3.** As Table 2, but for  $R_n$ .

	UCB	UMD	PAO	PRU	MPI	NCE	ERA	MER	GSW	NOA	CLM	MOS
UCB	0.0	22.5	-0.96	13.9	10.7	10.7	2.47	21.3	13.0	8.27	0.65	
UMD		22.5	-0.96	13.9	10.7	10.7	2.47	21.3	13.0	8.27	0.65	
PAO			-23.4	-8.60	-11.8	-11.8	-20.0	-1.21	-9.45	-14.2	-21.8	
PRU				14.8	11.6	11.7	3.43	22.2	14.0	9.23	1.61	
MPI					-3.20	-3.15	-11.4	7.39	-0.85	-5.60	-13.2	
NCE						0.05	-8.20	10.6	2.35	-2.40	-10.0	
ERA							-8.25	10.5	2.30	-2.45	-10.1	
MER								18.8	10.6	5.80	-1.82	
GSW									-8.24	-13.0	-20.6	
NOA										-4.75	-12.4	
CLM											-7.62	
MOS	<b>mean</b>											
UCB	0.0	28.8	27.2	24.7	29.2	21.5	22.9	27.4	27.6	24.7	23.6	
UMD		28.8	27.2	24.7	29.2	21.5	22.9	27.4	27.6	24.7	23.6	
PAO			31.7	19.4	27.2	21.4	28.1	16.4	27.2	28.8	32.5	
PRU				31.5	29.8	27.1	23.3	32.0	33.0	30.7	28.6	
MPI					28.6	18.2	23.9	20.9	28.2	26.4	29.6	
NCE						20.1	20.3	24.1	29.7	29.7	31.3	
ERA							17.8	18.5	25.7	23.9	26.4	
MER								25.7	30.5	27.6	27.6	
GSW									23.5	24.8	29.8	
NOA										12.7	17.4	
CLM											15.5	
MOS	<b>rmsd</b>											
UCB	1.00	0.94	0.92	0.92	0.92	0.94	0.93	0.95	0.92	0.92	0.92	
UMD		0.94	0.92	0.92	0.92	0.94	0.93	0.95	0.92	0.92	0.92	
PAO			0.96	0.95	0.94	0.95	0.95	0.96	0.91	0.91	0.92	
PRU				0.95	0.92	0.94	0.94	0.94	0.90	0.90	0.91	
MPI					0.94	0.96	0.96	0.95	0.90	0.92	0.92	
NCE						0.96	0.96	0.95	0.90	0.89	0.89	
ERA							0.97	0.96	0.91	0.92	0.92	
MER								0.96	0.89	0.90	0.90	
GSW									0.93	0.94	0.94	
NOA										0.98	0.98	
CLM											0.98	
MOS	<b>r<sup>2</sup></b>											

**Table 4.** Summary of the 1994  $Q_{le}$  (top),  $Q_h$  (middle), and  $R_n$  (bottom) correlation coefficients for each product (with respect to all the other products, and then presented here as an average of the individual correlations). The correlations are estimated for three cases: (1) the original monthly fluxes (all); (2) the inter-annual monthly fluxes (int); and (3) the deseasonalized monthly fluxes (des). See the text for more details.

	UCB	UMD	PAO	PRU	MPI	NCE	ERA	MER	GSW	NOA	CLM	MOS
	$Q_{le}$											
<b>all</b>	0.90	0.86	0.91	0.87	0.91	0.87	0.91	0.86	0.91	0.91	0.87	0.91
<b>int</b>	0.92	0.89	0.93	0.89	0.93	0.90	0.93	0.88	0.92	0.93	0.89	0.93
<b>des</b>	0.33	0.32	0.35	0.29	0.12	0.31	0.41	0.35	0.45	0.37	0.39	0.39
	$Q_h$											
<b>all</b>	0.82	0.81	0.88	0.80	0.86	0.81	0.86	0.78	0.85	0.86	0.85	0.83
<b>int</b>	0.83	0.83	0.89	0.82	0.88	0.83	0.88	0.81	0.86	0.88	0.86	0.84
<b>des</b>	0.31	0.28	0.34	0.18	0.11	0.32	0.38	0.35	0.37	0.26	0.33	0.31
	$R_n$											
<b>all</b>	0.94	0.94	0.94	0.93	0.94	0.93	0.95	0.94	0.95	0.93	0.93	0.93
<b>int</b>	0.96	0.96	0.96	0.95	0.95	0.94	0.96	0.95	0.96	0.94	0.95	0.95
<b>des</b>	0.45	0.45	0.40	0.33	0.12	0.26	0.40	0.32	0.33	0.32	0.34	0.32

**Table 5.** 1994 monthly mean  $Q_{le}$  normalized RMS difference for each vegetation class. For each product the statistics are calculated with respect to all the other products, and then product-averaged to get one estimate per product and class. Normalization is done by dividing the products difference by the average of the product fluxes.

	UCB	UMD	PAO	PRU	MPI	NCE	ERA	MER	GSW	NOA	CLM	MOS
<b>RaFo</b>	0.22	0.27	0.24	0.24	0.21	0.26	0.20	0.37	0.25	0.24	0.27	0.23
<b>EvFo</b>	0.46	0.43	0.43	0.52	0.41	0.60	0.37	0.49	0.48	0.42	0.54	0.43
<b>DeFo</b>	0.42	0.41	0.40	0.52	0.39	0.53	0.35	0.51	0.41	0.39	0.51	0.42
<b>EvWo</b>	0.59	0.60	0.54	0.68	0.55	0.70	0.49	0.61	0.62	0.55	0.70	0.57
<b>DeWo</b>	0.40	0.43	0.36	0.37	0.35	0.46	0.34	0.43	0.41	0.39	0.53	0.42
<b>Cult</b>	0.39	0.38	0.33	0.50	0.37	0.44	0.33	0.42	0.36	0.34	0.46	0.38
<b>Gras</b>	0.45	0.50	0.42	0.55	0.48	0.51	0.42	0.55	0.43	0.42	0.54	0.46
<b>Tund</b>	0.80	0.68	0.74	0.89	0.66	0.88	0.59	0.74	0.72	0.81	0.84	0.70
<b>Shru</b>	0.61	0.61	0.52	0.71	0.60	0.64	0.53	0.79	0.54	0.54	0.64	0.56
<b>Dese</b>	1.04	1.50	0.86	1.35	1.33	0.92	1.01	0.99	0.90	1.01	1.05	0.91

**Table 6.** Correlation coefficients between the monthly mean  $Q_{le}$  and  $R_n$  for the different products and vegetation classes for Dec-Jan-Feb 1994 (DJF)(top) and Jul-Aug-Sep 1994 (JAS)(bottom). Only pixels with latitude  $> -20^\circ$  are considered. AmFo gives the correlations for the Amazonian rain forest pixels. The last column gives the class averaged precipitation in  $mm\ day^{-1}$ .

	UCB	UMD	PAO	PRU	MPI	NCE	ERA	MER	GSW	NOA	CLM	MOS	prec
<b>DJF</b>													
<b>RaFo</b>	0.82	0.74	0.50	0.85	0.55	0.72	0.54	0.12	0.42	0.57	0.05	0.47	7.08
<b>EvFo</b>	0.95	0.91	0.98	0.92	0.96	0.89	0.95	0.95	0.94	0.92	0.76	0.91	1.55
<b>DeFo</b>	0.94	0.90	0.97	0.93	0.95	0.91	0.96	0.94	0.91	0.93	0.76	0.93	1.42
<b>EvWo</b>	0.95	0.98	0.94	0.91	0.95	0.87	0.95	0.93	0.91	0.90	0.85	0.89	1.83
<b>DeWo</b>	0.94	0.97	0.93	0.92	0.94	0.89	0.92	0.87	0.87	0.84	0.79	0.85	3.08
<b>Cult</b>	0.92	0.91	0.93	0.92	0.91	0.83	0.92	0.91	0.86	0.85	0.70	0.84	1.73
<b>Gras</b>	0.84	0.91	0.86	0.85	0.86	0.82	0.88	0.82	0.82	0.71	0.66	0.73	1.86
<b>Tund</b>	0.93	0.61	0.91	0.78	0.87	0.03	0.67	0.79	0.48	0.21	0.70	0.60	0.84
<b>Shru</b>	0.90	0.90	0.87	0.87	0.88	0.79	0.85	0.80	0.77	0.72	0.72	0.76	1.19
<b>Dese</b>	0.64	0.51	0.50	0.73	0.40	0.49	0.48	0.49	0.28	0.28	0.28	0.26	0.30
<b>AmFo</b>	0.91	0.78	0.86	0.90	0.78	0.85	0.60	-0.25	0.44	0.64	0.14	0.54	7.75
<b>JAS</b>													
<b>RaFo</b>	0.88	0.81	0.84	0.91	0.71	0.46	0.67	0.67	0.58	0.71	0.54	0.65	4.74
<b>EvFo</b>	0.96	0.93	0.92	0.90	0.88	0.63	0.78	0.74	0.82	0.83	0.54	0.76	3.37
<b>DeFo</b>	0.96	0.95	0.95	0.93	0.92	0.68	0.87	0.77	0.84	0.89	0.69	0.89	3.41
<b>EvWo</b>	0.86	0.94	0.84	0.88	0.81	0.48	0.84	0.61	0.72	0.68	0.46	0.57	1.89
<b>DeWo</b>	0.51	0.84	0.65	0.78	0.72	0.36	0.50	0.34	0.51	0.42	0.18	0.12	2.40
<b>Cult</b>	0.76	0.75	0.72	0.80	0.81	0.42	0.70	0.61	0.55	0.50	0.49	0.54	3.57
<b>Gras</b>	0.52	0.50	0.61	0.64	0.85	0.41	0.58	0.57	0.51	0.20	0.37	0.34	2.28
<b>Tund</b>	0.98	0.95	0.96	0.92	0.96	0.85	0.96	0.91	0.86	0.77	0.79	0.93	2.05
<b>Shru</b>	0.48	0.49	0.54	0.53	0.77	0.47	0.49	0.58	0.35	0.11	0.18	0.24	1.11
<b>Dese</b>	0.38	0.36	0.61	0.63	0.56	0.54	0.69	0.75	0.31	0.11	0.21	-0.23	0.73
<b>AmFo</b>	0.88	0.82	0.88	0.94	0.75	0.28	0.67	0.78	0.58	0.73	0.54	0.63	4.80



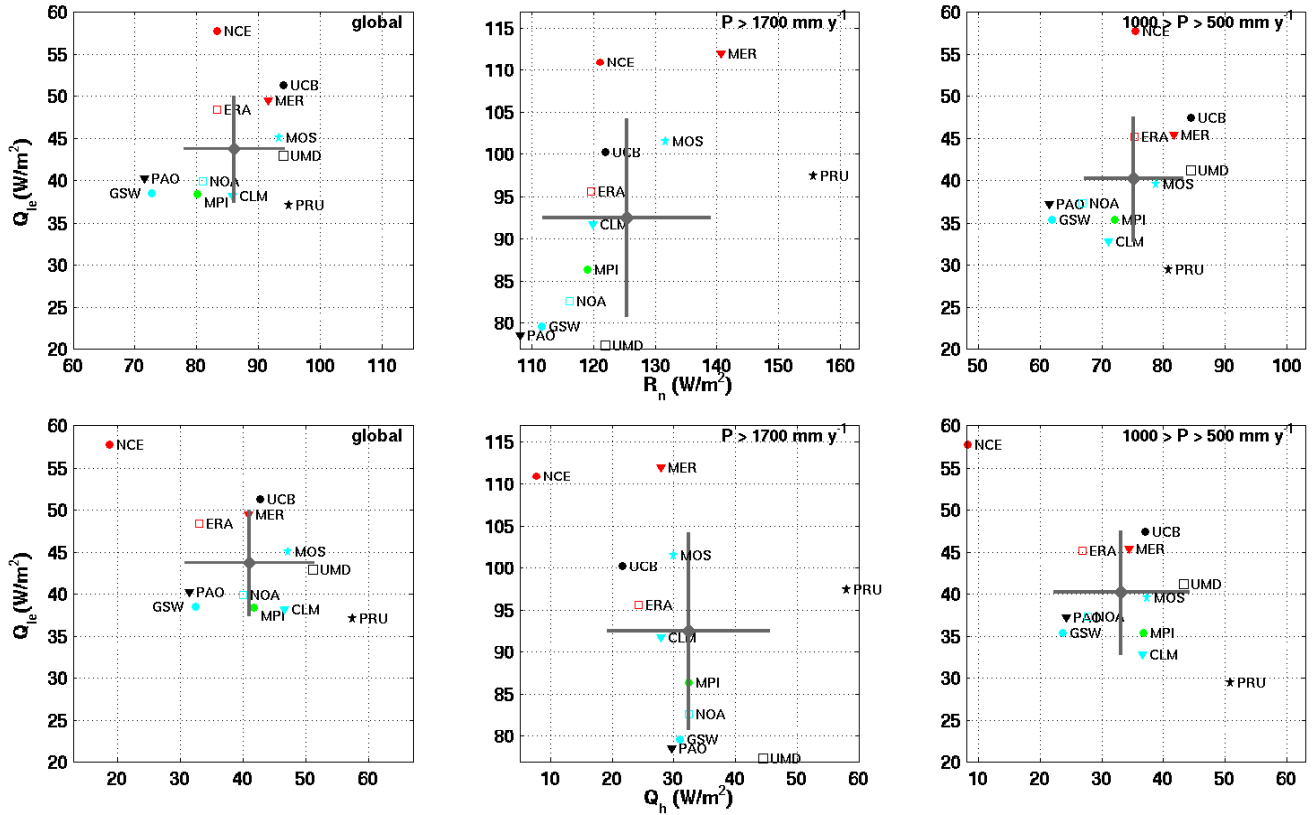


**Figure 1.**  $Q_{le}$  annual means as a function of the  $R_n$  (top) and  $Q_h$  (bottom) annual means for the year 1994. The averages are plotted for all the globe (left), for the regions where  $P > 1700 \text{ mm year}^{-1}$  (middle), and for  $500 < P < 1000 \text{ mm year}^{-1}$  (right). The grey dot and lines display respectively the ensemble mean and the standard deviation ( $\pm\sigma$ ) of the individual product annual means around the ensemble mean.

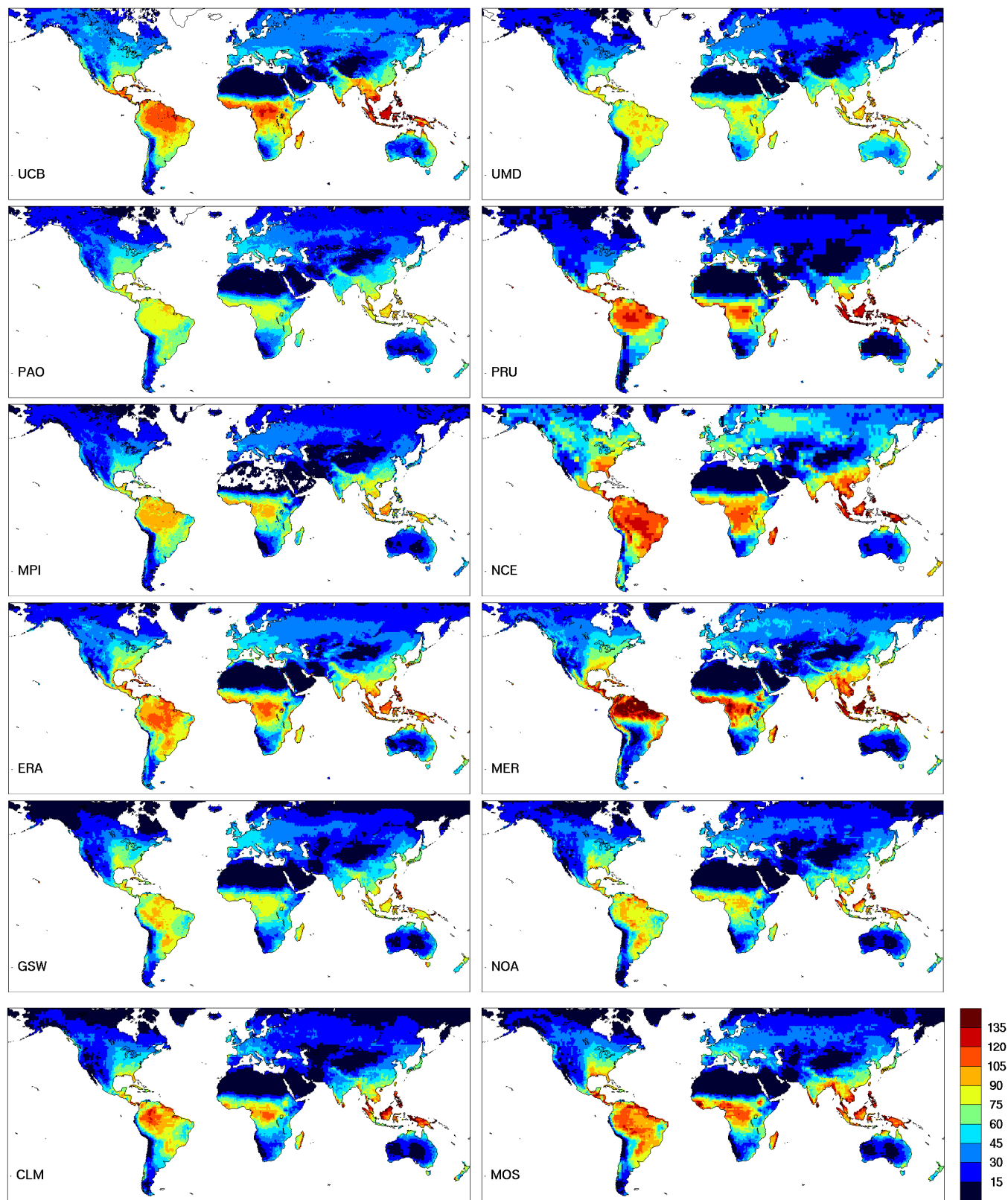
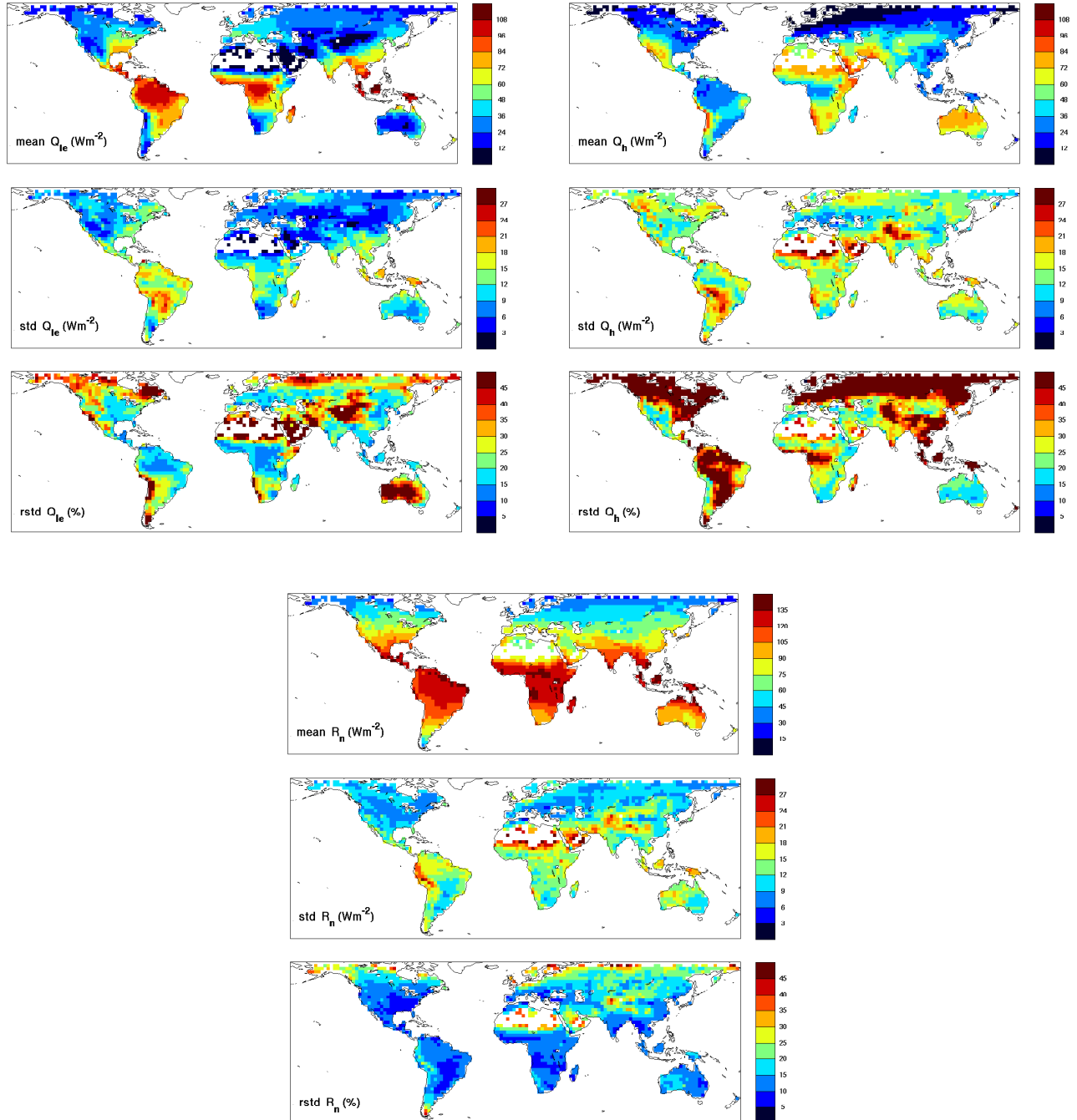
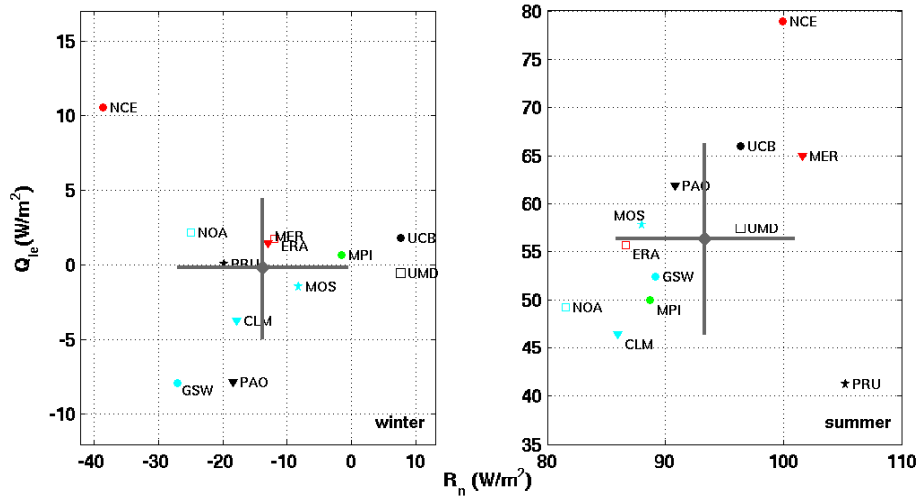


Figure 2. 1994 yearly averaged  $Q_{le}$  ( $W m^{-2}$ ).



**Figure 3.** 1994 all-product ensemble mean (mean), standard deviation (std), and relative standard deviation (rstd)(expressed as a percentage of the pixel mean value) for  $Q_{le}$  (top-left),  $Q_h$  (top-right), and  $R_n$  (bottom). Absence of data from some products precludes the computation of the averages at some regions, mainly over Northern Africa.



**Figure 4.**  $Q_{le}$  means as a function of the  $R_n$  means for snow-covered regions in Dec–Jan–Feb 1994 (left) and for the same regions in Jul–Aug–Sep 1994 (right). The grey dot and lines display respectively the ensemble mean and the standard deviation ( $\pm\sigma$ ) of the individual product annual means around the ensemble mean.

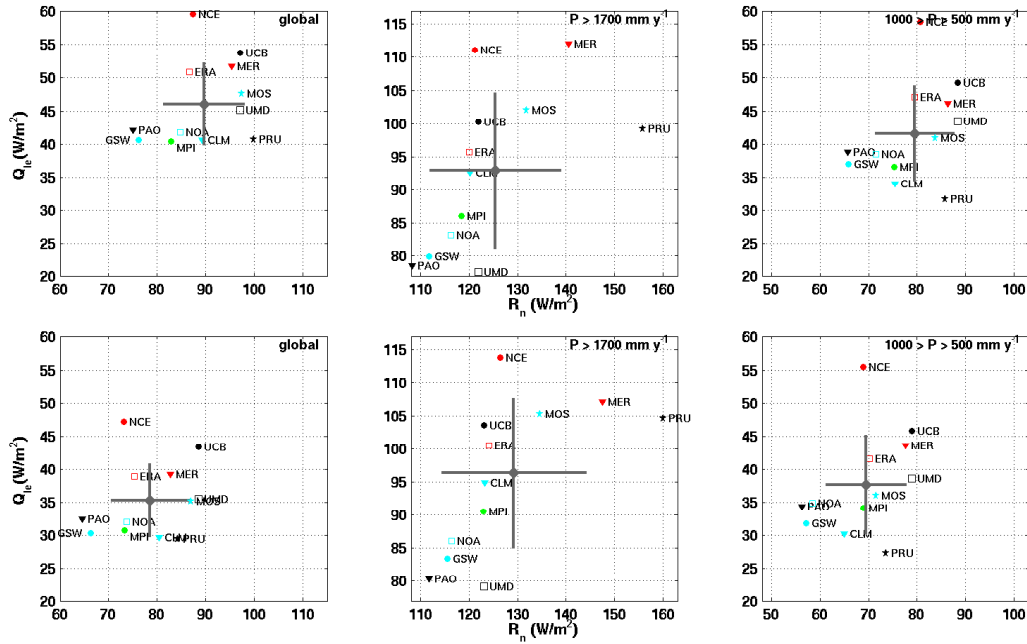


**Figure 5.** As the  $Q_{le}$  versus  $R_n$  plots of Figure 1 (products aggregated onto a  $2.5^\circ \times 2.5^\circ$  grid), but here with (top panels) products re-gridded into an equal area grid of  $\sim 770 \text{ km}^2$  with a lat-lon box of  $\sim 0.25^\circ \times 0.25^\circ$  at the equator; and (bottom panels) again onto the  $2.5^\circ \times 2.5^\circ$  grid, but only for pixels that do not include water bodies, according to a classification derived from a satellite product.

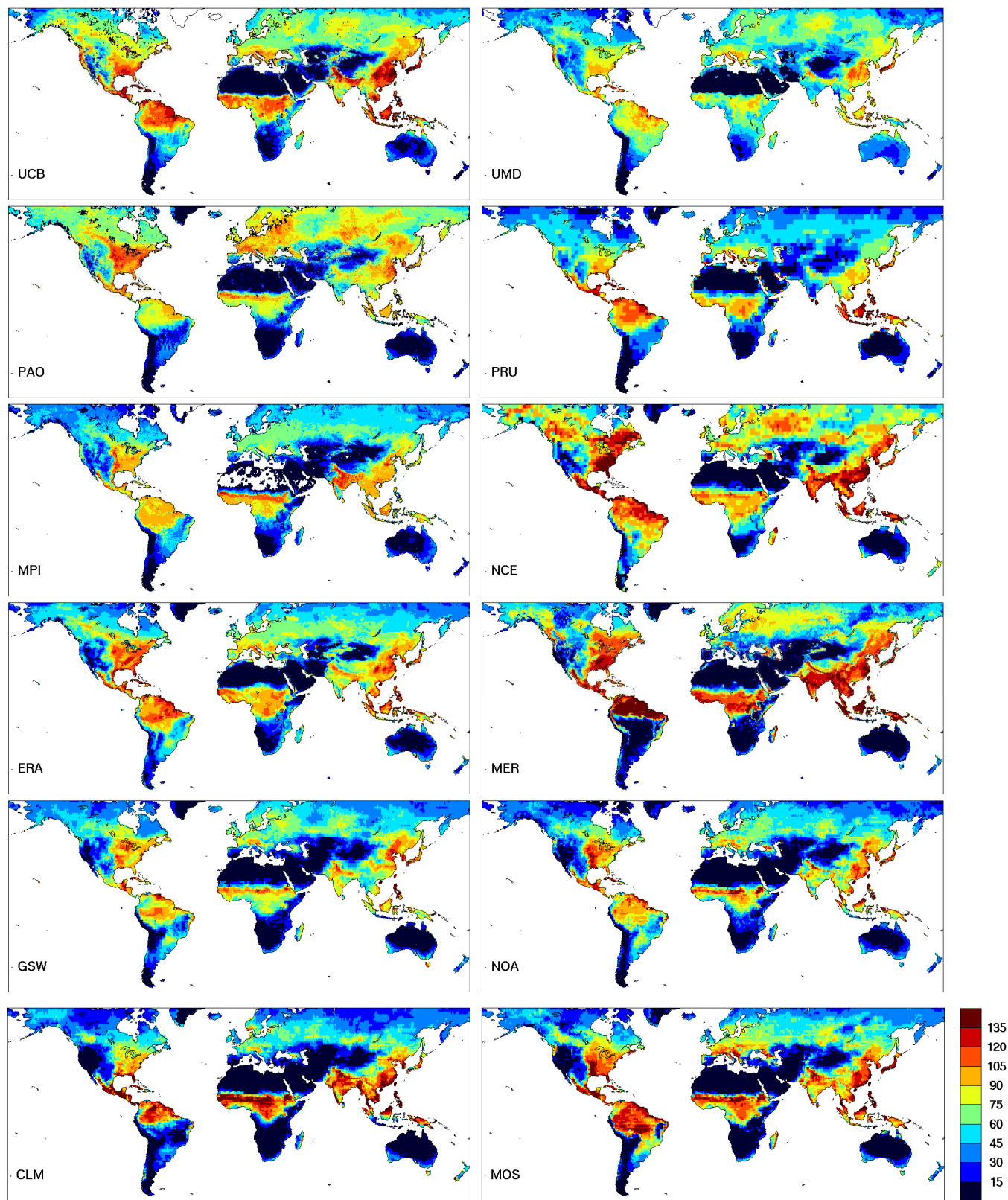


Figure 6. Monthly averaged  $Q_{1e}$  for August 1994 ( $W m^{-2}$ ).



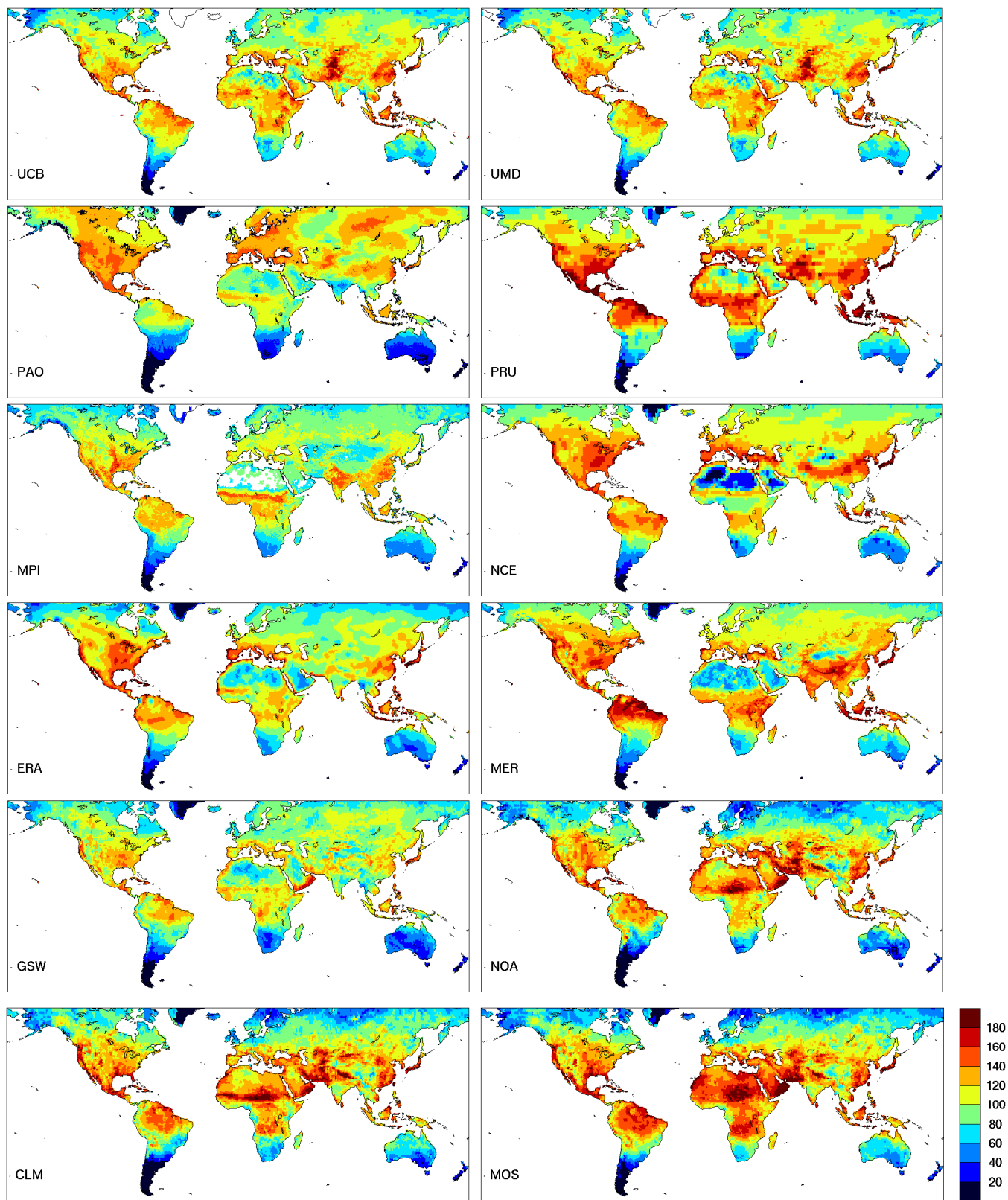
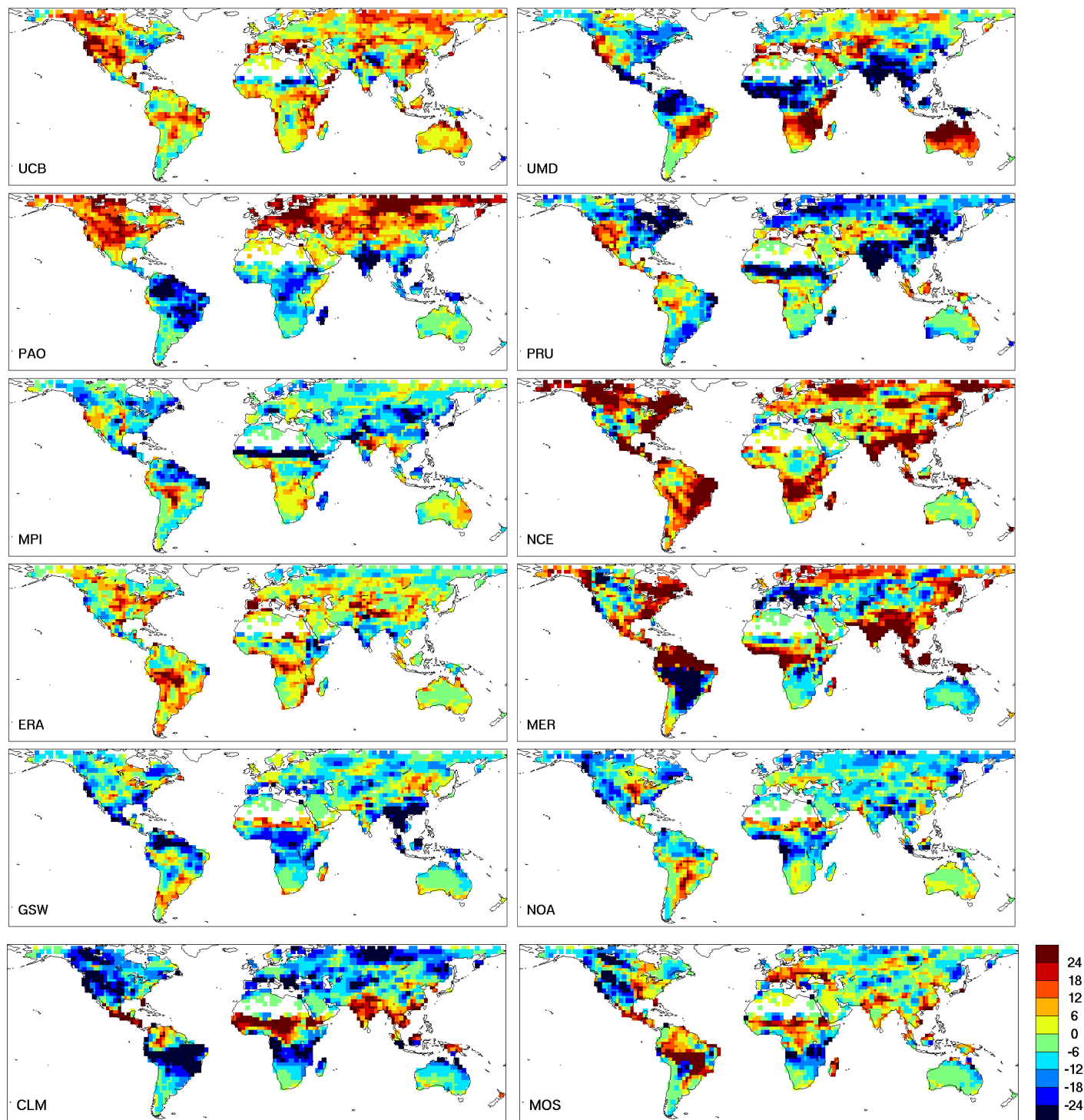
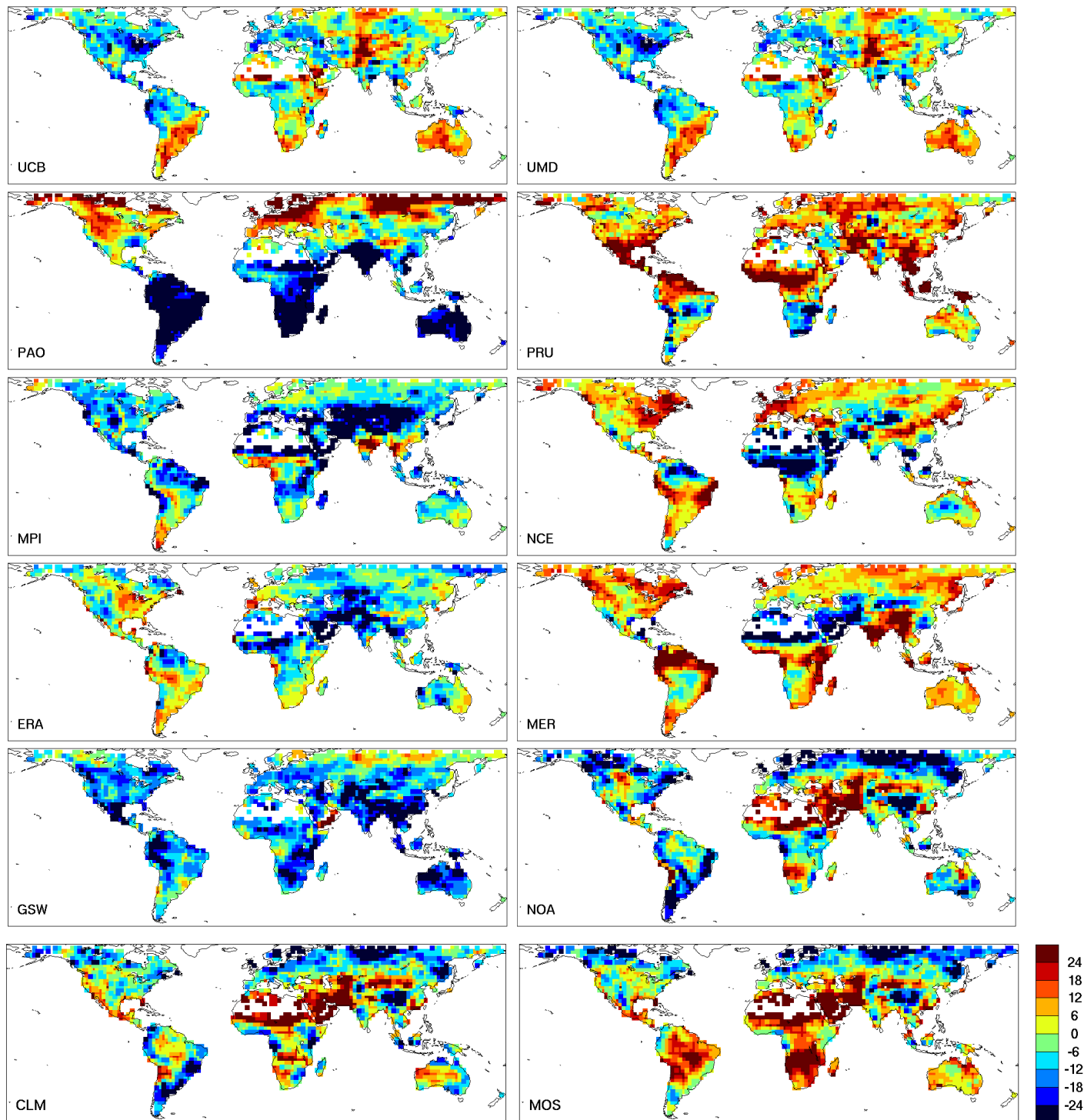


Figure 7. Monthly averaged  $R_N$  for August 1994 ( $W m^{-2}$ ).



**Figure 8.** Monthly averaged  $Q_{1e}$  differences for August 1994 between the products and the all-product ensemble mean ( $W m^{-2}$ ).





**Figure 9.** Monthly averaged  $R_n$  differences for August 1994 between the products and the all-product ensemble mean ( $W m^{-2}$ ).

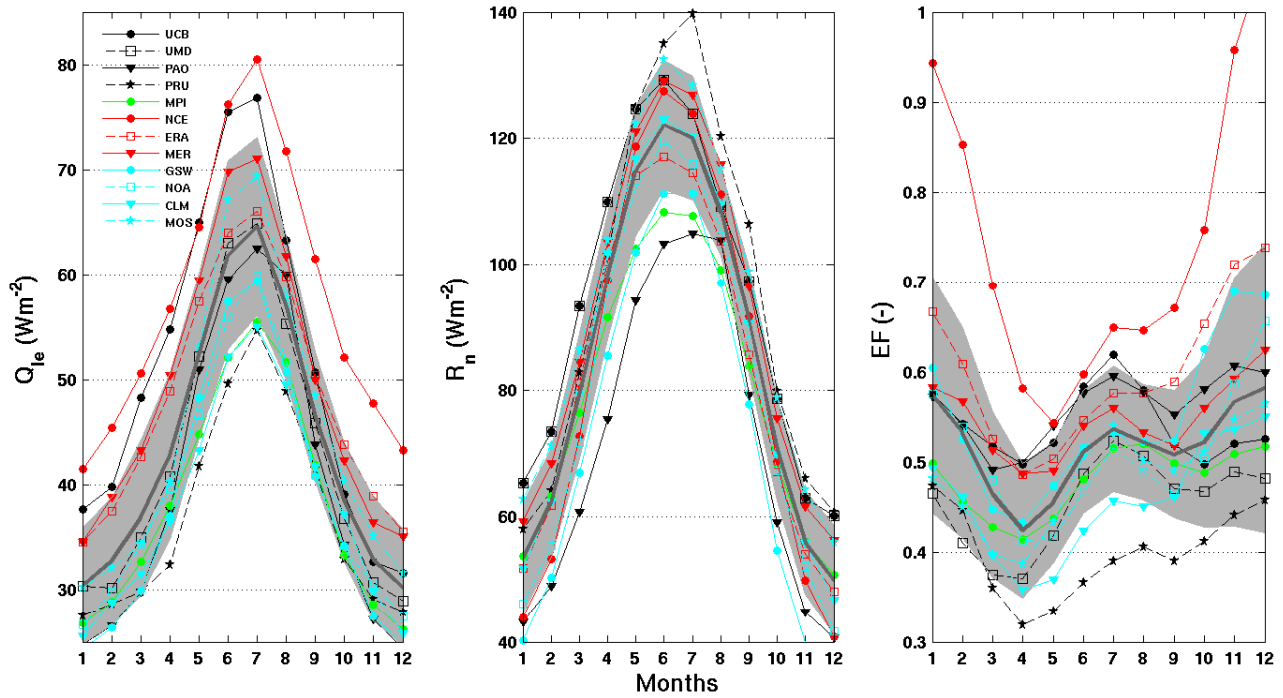


**Figure 10.** Global 1994 annual cycles of  $Q_{le}$  (left),  $R_n$  (middle), and  $EF$  (right). The grey line and shadow display respectively the ensemble mean and the standard deviation ( $\pm\sigma$ ) of the individual product monthly means around the ensemble mean.

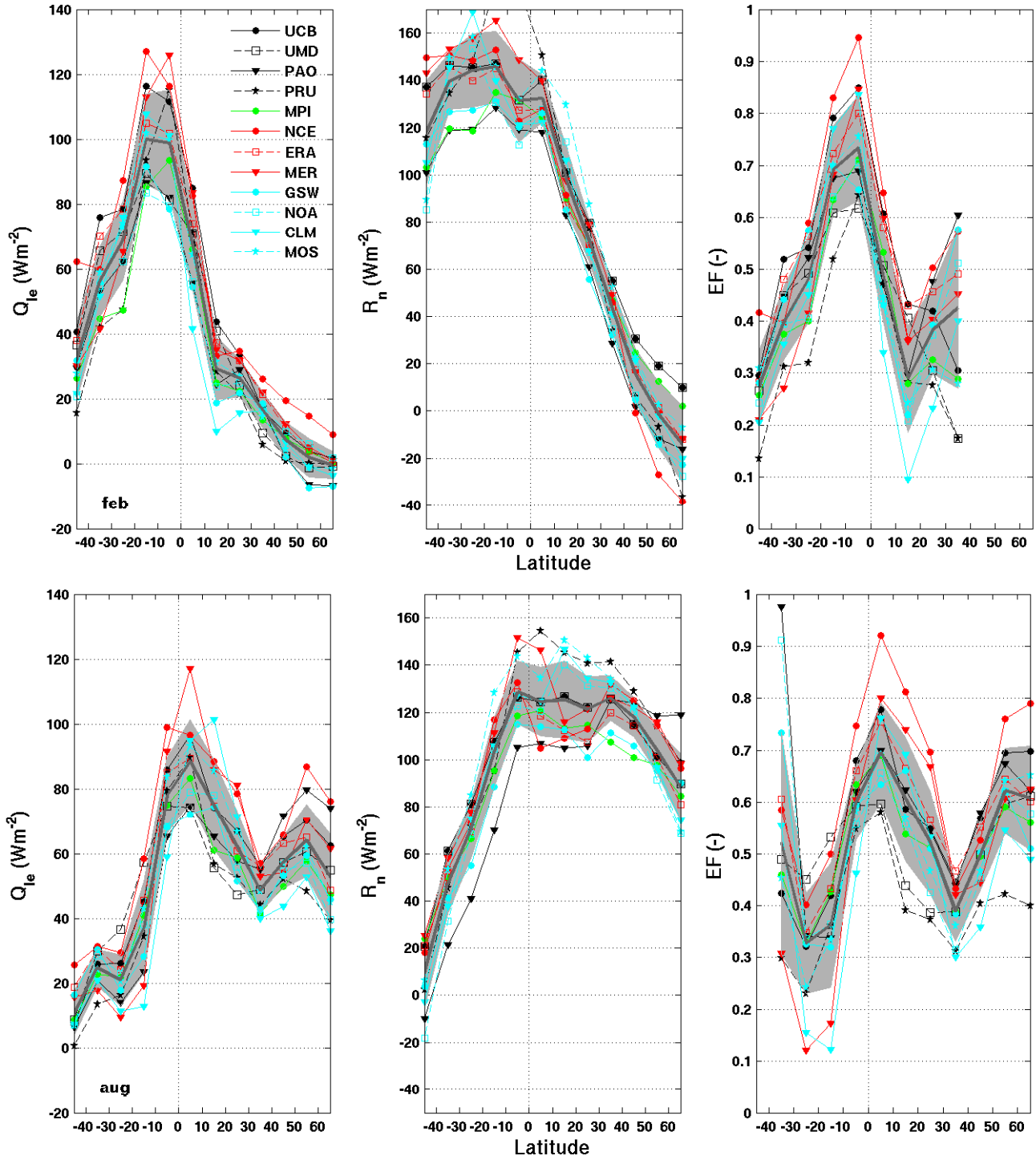


Figure 11. Zonal means of  $Q_{le}$  (left),  $R_n$  (middle), and  $EF$  (right) for February (top) and August (bottom) 1994. The grey line and shadow display respectively the ensemble mean and the standard deviation ( $\pm\sigma$ ) of the individual product annual means around the ensemble mean.

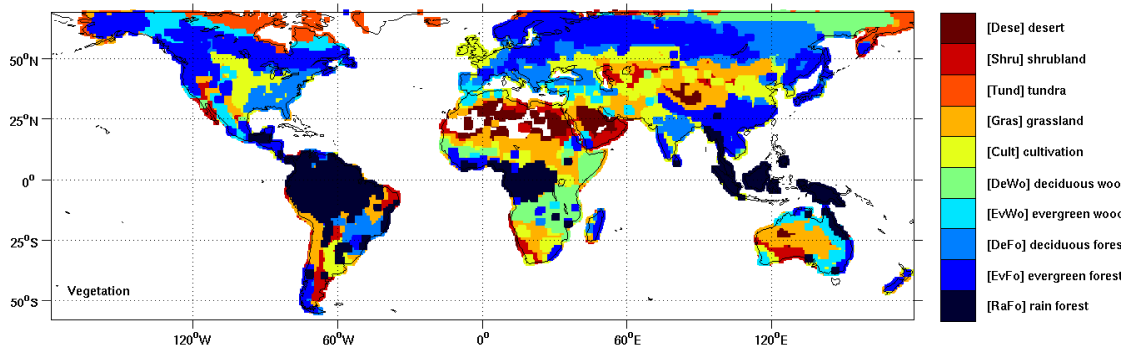
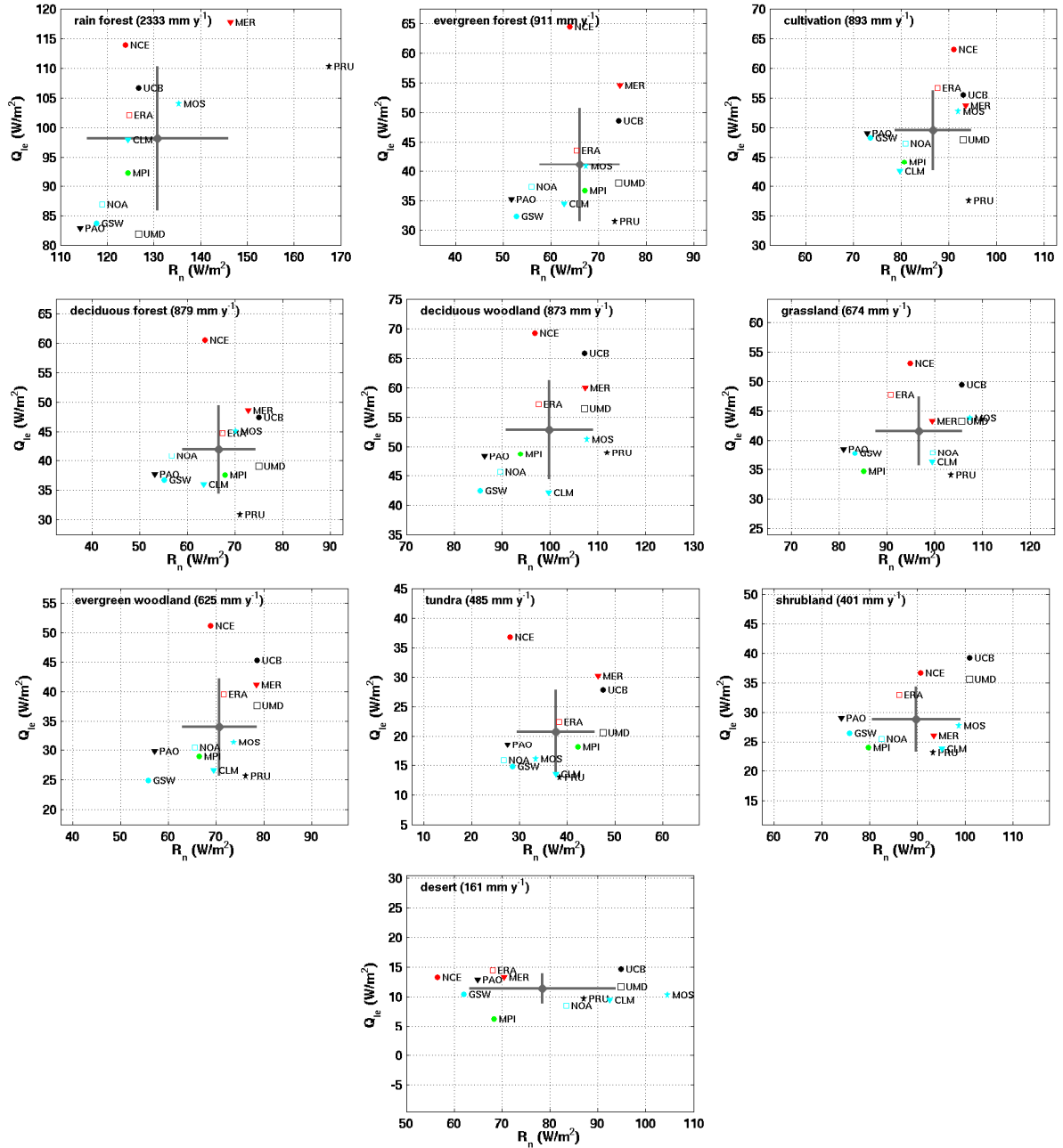


Figure 12. Geographical location of vegetation classes considered in the study.



**Figure 13.** 1994 spatially averaged  $Q_{le}$  annual mean as a function of the  $R_n$  annual mean for different vegetation classes. The class averaged annual mean precipitation is given close to the class name. The axes scales are different for each class, but they span the same range. The grey dot and lines display respectively the ensemble mean and the standard deviation ( $\pm\sigma$ ) of the individual product annual means around the ensemble mean.

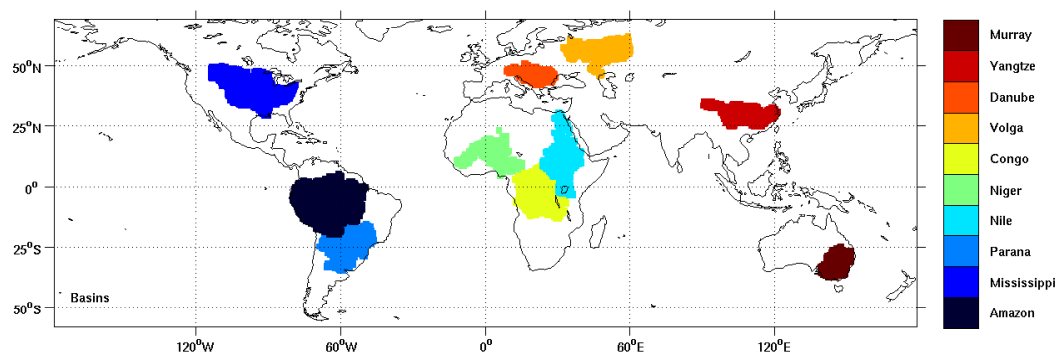
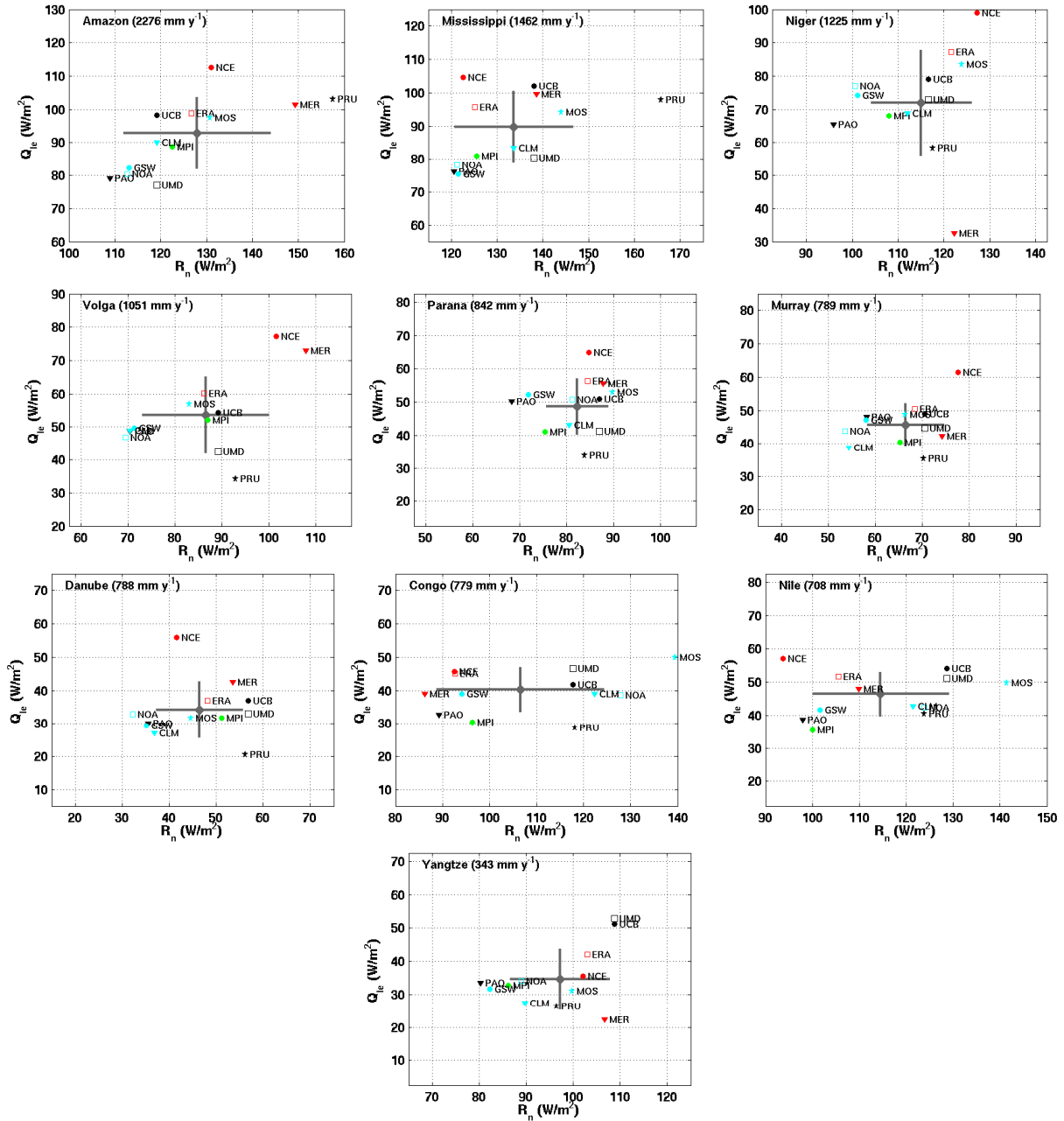


Figure 14. Geographical location of basin areas considered in the study.



**Figure 15.** Basin averaged  $Q_{le}$  annual mean as a function of the  $R_n$  annual mean for the year 1994. The basin averaged annual mean precipitation is given close to the basin name. The axes scales are different for each basin, but they span the same range. The grey dot and lines display respectively the ensemble mean and the standard deviation ( $\pm\sigma$ ) of the individual product annual means around the ensemble mean.

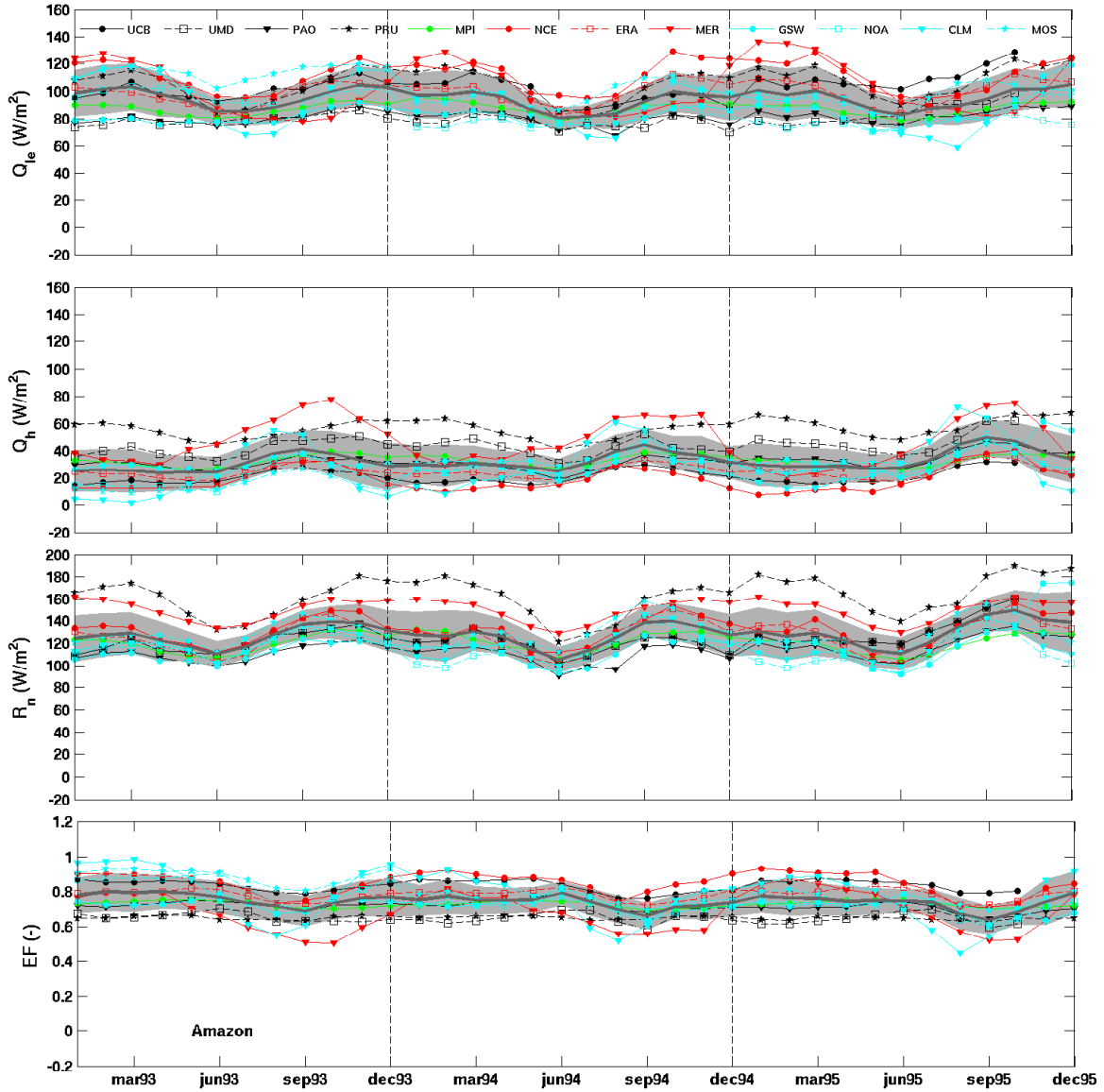


Figure 16. Spatially averaged monthly time series for the Amazon basin. From top to bottom:  $Q_{le}$ ,  $Q_h$ ,  $R_n$ , and EF.



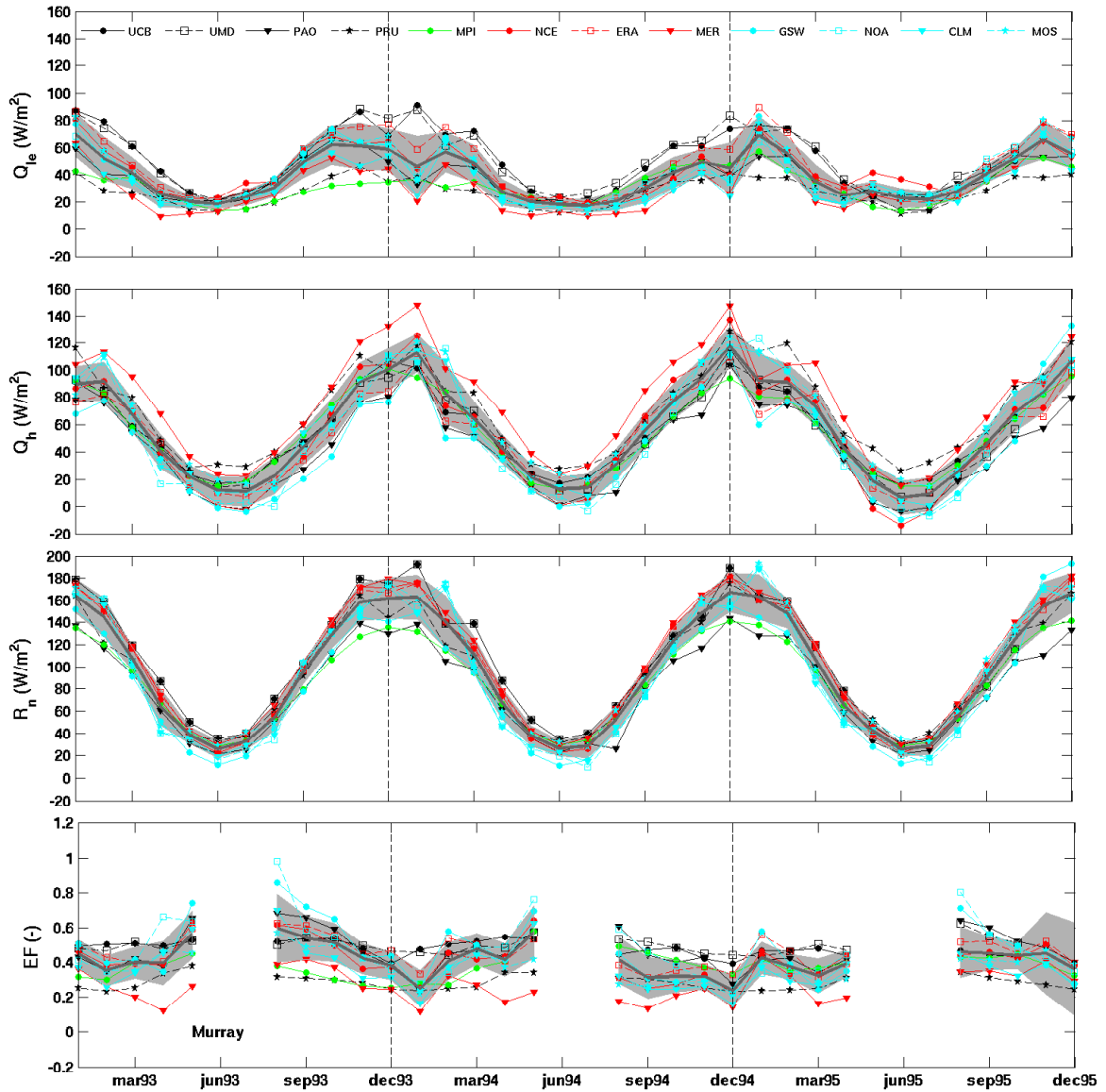


Figure 17. As Figure 16, but or the Murray basin.